Thin Solid Films 744 (2022) 139083

Contents lists available at ScienceDirect

Thin Solid Films

journal homepage: www.elsevier.com/locate/tsf

Thin films made by reactive sputtering of high entropy alloy FeCoNiCuGe: Optical, electrical and structural properties

J. Mayandi [a,b,c], T.G. Finstad [a,b,*], Ø. Dahl [d], P. Vajeeston [b,e], M. Schrade [a,f], O.M. Løvvik [a,f], S. Diplas [e,f], P.A. Carvalho [f,g]

[a] Department of Physics, University of Oslo, 0316 Oslo, Norway
[b] Centre for Materials Science and Nanotechnology, University of Oslo, 0318 Oslo, Norway
[c] Department of Materials Science, School of Chemistry, Madurai Kamaraj University, Madurai, 625021, India
[d] SINTEF Industry, Department of Materials and Nanotechnology, 7034 Trondheim, Norway
[e] Department of Chemistry, University of Oslo, 0315 Oslo, Norway
[f] SINTEF Industry, Department of Sustainable Energy Technology, 0373 Oslo, Norway
[g] CeFEMA, Instituto Superior Técnico (IST), Universidade de Lisboa, Lisboa 1049-001, Portugal

ARTICLE INFO

Keywords:
High entropy alloy
Thin films
High entropy oxide
Electrical properties
Sputter depositions

ABSTRACT

Films were reactively sputtered from a high entropy alloy (HEA) FeCoNiCuGe target in an Ar/O_2 plasma. The case of zero O_2 gas flow yielded HEA films of FeCoNiCuGe. These as-deposited HEA films have a face centered cubic (FCC) structure, showing a texture with columnar grains containing many planar defects. The residual electrical resistivity of the films is around 225 μΩcm and the temperature dependence of the resistivity is metal-like. The temperature coefficient of resistivity is small (4.5 ppm/K). The Hall coefficient is positive while the Seebeck coefficient is negative. This is interpreted as arising from an electronic structure having both holes and electrons at the Fermi level as indicated by band structure calculations. The HEA FCC structure is unstable upon annealing in forming gas and showed demixing. Annealing in O_2 also yielded inhomogeneous oxides, with a thick layer of CuO growing on the surface. The cases of reactive sputtering with an oxygen flow yielded oxides that are either nanocrystalline or amorphous dependent upon the sputter conditions. These can be classified as high entropy oxides (HEO) and have an optical bandgap around 1.9 eV and high transmission in the infrared region. The amorphous HEO has an electrical conduction interpreted as due to variable range hopping described by the Efros–Shklovskii theory. The HEO films were reduced in forming gas. For the amorphous HEO film, the reduction at 300–500 °C yielded hexagonal Ni_5Ge_2 and an FCC phase. For the nanocrystalline HEO, reduction resulted in creation of FCC and body centered cubic HEA metal phases.

1. Introduction

High entropy alloys (HEA) have been given increased attention in materials science communities by introducing concepts for phase stability and opening up opportunities at the frontiers of material design for structural, industrial and technological applications [1–5]. Most work has been done within metallurgy. Traditional alloy design in metallurgy usually uses one majority component as the basis and then adds small amounts of various elements to engineer the properties. HEA are alloys containing many elements, typically at least 5, at high concentrations close to equiatomic proportions [6]. Application possibilities open up when the alloy has favorable characteristics and can be engineered. The entropy of mixing has been considered to stabilize these alloys [1]. Several of the transition metal HEA systems that have been reported show single-phase or dual-phase solid solution phases, without the formation of intermetallic compounds, that are otherwise observed for many traditional metal alloy systems [7]. The reported solid solution phases have simple crystal structures being face centered cubic(FCC) or body centered cubic(BCC). The high configurational entropy of mixing was at first considered the key to this stabilization of the alloy systems. However, the high stability of some HEA systems cannot be justified by the configurational entropy alone and it has been argued that the vibrational, magnetic and electronic entropy play an equally large role [8, 9]. Many HEAs were initially reported as solid solutions, but

* Corresponding author:.
E-mail address: terje.finstad@fys.uio.no (T.G. Finstad).

https://doi.org/10.1016/j.tsf.2022.139083
Received 27 April 2021; Received in revised form 30 December 2021; Accepted 3 January 2022
Available online 5 January 2022

according to Schneeweiss et al. [10] secondary phases are the rule rather than the exception, among the HEA systems studied.

There has been a recent increased interest in high entropy oxides (HEO) [11–14], following the demonstration that, among many oxide candidates tested, the oxide ($Mg_{0.2}Co_{0.2}Ni_{0.2}Cu_{0.2}Zn_{0.2}$)O, called J14 [15] could be stabilized by entropy. HEO systems consist of four or more cation elements in equiatomic concentrations on one of the sublattices in simple oxide structures [16]. Different oxide systems have been explored and grouped into transition metal oxides, and rare-earth oxides. Most of the HEO structures reported have simple crystal structures like rock salt [15, 17], fluorite [18], spinel [19] or perovskite [16]. The main given reason for the growing interest in HEO is the potential to obtain favorable properties by exploiting the enormous number of possible elemental combinations.

In the present study the HEA is FeCoNiCuGe. The transition metal atoms Fe, Co, Ni and Cu in the alloy are among the most studied elements in HEAs, while Ge is chemically distinct from the other elements, but has similar atomic radius. Previously, Braeckman et al. [20] studied the incorporation of various amounts of Ge in CrFeCoNiCu films and reported on the phases and structural characteristics of the films. It was reported that the CrFeCoNiCu film system with no Ge yields a single FCC phase as expected from other reports on that system [9, 21-23]. For Ge concentrations above 15 at.%, Braeckman et al. [20] reported an amorphous structure. Here we report on sputter-deposited FeCoNiCuGe films and present measurements on their structure, their low temperature electric resistivity, and the stability upon annealing in different ambient gasses. Since the films have been produced by sputtering, which is a nonequilibrium process, the as-deposited structure may be metastable. Hence, structural stability is investigated by annealing to make the equilibrium state kinetically accessible. We further explore the effect of sputtering from a HEA target in a plasma with different concentrations of oxygen. We do form films containing oxygen and report on their structure, stability, electrical properties, and optical transmission.

2. Experimental methods and sample preparation

The films were sputter deposited in an AJA International Inc. ATC-2200 sputtering system using a 50.8 mm diameter target of the alloy FeCoNiCuGe having equiatomic composition. The material was arc melted by Goodfellow Cambridge Ltd and machined to a target by our workshop. The deposition chamber was powered by an AJA 100/300 RF generator (13.56 MHz) with an automatic impedance matching unit. The system has a confocal target-substrate geometry with a target-substrate distance of ~15 cm. Rotation of the substrate was used to achieve uniform deposition over the 100 mm diameter substrates. These were made of fused silica, which was chosen due to suitability for electrical and optical characterization of the deposited films. The base pressure in the system was 5×10^{-5} Pa. The flow of Ar and O_2 gas for reactive sputtering was controlled by mass flow controllers (MKS Instruments) and set to 67 SCCM(standard cubic centimeter per minute) flow of Ar for inert sputtering, and 65 SCCM Ar plus 2 SCCM of O_2, or 57 SCCM Ar plus 10 SCCM of O_2 for reactive sputtering. The total pressure during deposition was measured with a Baratron capacitance manometer (MKS Instruments) and set to 0.6 Pa through the gate valve with a VAT PM-5 adaptive pressure controller.

Three different sputtering runs with systematically different oxygen ambient are reported here. For easy reference these are given different sample symbols, S0, S3 and S15, respectively, where the digits signify the oxygen flow ratio in percentage. The sputter parameters for the three deposition-conditions are listed in Table 1. After deposition, the wafers were cleaved into individual samples, typically 1 × 1 cm. They were characterized as-deposited (ASD) and after furnace annealing in flowing gas of either O_2 or a N_2:H_2 (90:10) mixture (NHM) at temperatures of 300, 400 or 500 °C for 2 h.

The films were characterized by scanning transmission electron microscopy (STEM/TEM), using imaging, energy dispersive spectroscopy (EDS) and selected area electron diffraction (SAD) of the film cross-sections. These techniques were carried out at 300 kV with an FEI Titan G260-300 instrument equipped with a DCOR probe corrector and a Super-X Bruker energy dispersive spectrometer with 4 silicon-drift detectors. Imaging was performed with a probe current of ≈150 pA and nominal spatial resolution of 0.08 nm. The specimens were prepared by focused ion beam (Ga^+) with an FEI Helios G4 dual-beam instrument using 30 keV ions for the deep milling and 2 keV ions for the final polishing. The crystal structure of the thin films was also analyzed by X-ray diffraction (XRD) using a Bruker AXS D8 Discover Diffractometer with Cu Kα radiation (λ= 1.5418 Å in a standard Bragg-Brentano θ−2θ configuration at room temperature (RT). Rutherford Backscattering Spectrometry (RBS) of alpha particles in a tandem accelerator (NEC 4000) was used to measure the oxygen concentration. The concentration value reported for each case represents the best estimated value for the specified sample with a best estimate of the uncertainty arising mostly from the uncertainty in the method for the particular case. Some samples were characterized by Secondary Ion Mass Spectroscopy (SIMS) using a Cameca IMS 7f instrument with a primary beam of 10 keV O^{+2} or 15 keV Cs^+ ions. Qualitative concentration versus depth profiles were recorded to a depth just exceeding the substrate interface. The samples were also characterized using scanning electron microscopy (SEM, here FEI Quanta 200 FEG-ESEM).

The optical transmittance of the sputtered thin films was measured in the 290 nm - 2500 nm range using a spectrophotometer from Shimadzu SolidSpe-3700 DUV. A LakeShore Hall system, model 7604, was used to measure electrical parameters such as resistivity, carrier concentration and Hall mobility as a function of magnetic field (1000 G to 10,000 G) and temperature (10 K – 300 K). The Seebeck coefficient was measured in a custom-built setup [24].

Table 1
Sputter deposition parameters for sample S0 S3 and S15.

Sample	RF Power (W)	Pressure (Pa)	VDC (V)	Time min.	q_{Ar} (SCCM)	q_{O_2} (SCCM)	Flow ratio %
S0	100	0.67	440	130	67	0	0
S3	150	0.67	198	90	65	2	3
S15	150	0.67	265	90	57	10	15

(q_{Ar} and q_{O_2} is the of flow rate for Ar and O_2 gas respectively in units of standard cubic centimeters per minute(SCCM). The flow rate ratio is $q_{O_2}/(q_{O_2}+q_{Ar}) \times 100\%$. V_{DC} is the voltage between target and substrate.).

3. Results and discussion

The experimental data are presented according to characterization technique, then divided between sample S0, S3 and S15 (see Table 1), and then according to heat treatment environment and temperature. Table 2 shows parameters and results for S0, S3 and S15 ASD. The experimental data are discussed throughout Section 3, containing many forward pointers to sub sections. Results and their discussions are summarized in Section 3.8 and also put in a wider perspective.

Table 2
Characteristics of the samples S0, S3 and S15 ASD.

Sample	Thickness (nm)	Oxygen conc (at.%)	Structure	Resistivity (Ωcm)	Bandgap (eV)
S0	193	6 ± 5	FCC	2.52×10^{-4}	0
S3	343	59 ± 5	amorph.	80	1.9
S15	280	62 ± 5	nanoXtal	high($>10^8$)	1.9

The oxygen concentration was measured by RBS. The thickness was measured by STEM / EDS. The structure was determined by XRD and TEM. The resistivity was measured at RT. The bandgap comes from optical transmission measurements.

3.1. TEM and stem characterization

3.1.1. Sample S0 ASD

Fig. 1 shows STEM cross sectional images of film S0. It is seen that the film consists of columnar grains extending through the film thickness. The typical column diameter is in the 10–20 nm range (see Fig. 1(f)). The EDS element maps in Fig. 3 indicate a uniform element concentration throughout the film, and their quantification shown in Table 3 indicates near equiatomic concentration.

Fig. 2 shows a SAD pattern from film S0. It has characteristics that are interpreted as corresponding to a nanocrystalline FCC structure with a weak preferred crystallographic orientation. The experimental diffraction pattern has been superimposed in Fig. 2(b) with calculated diffractograms (In 1D and 2D using the crystal structure (A1, $Fm\bar{3}m$, # 225).The many lines in Fig. 1(f) result from the presence of many planar defects identified as mirror planes parallel to {111}, and is also consistent with streaks in the diffraction pattern. Grown FCC metal films often have Σ3{111} twin boundaries, where every 3rd lattice site on the boundary is shared [25]. This coherent twin boundary is where the atomic stacking switches from the abcabcabc stacking of {111} planes to abcabacba, where the second b is the twinning plane. The boundary itself can also be seen as a stacking fault (when approached from either direction).

So, the studied film specimen consists of a single-phase alloy with near equiatomic concentration having an FCC crystal structure with nanometric coherency length. We will compare with XRD presented in Section 3.1.2. but mention here that the agreement indicates that the above structure is not a result of the TEM specimen preparation using FIB. We will discuss the existence of a single-phase FCC structure in Section 3.8.2 and discuss its grain size in Section 3.8.1.

3.1.2. Sample S3 ASD

Fig. 3 shows cross-sectional STEM images of S3 ASD. Fig. 3(a) shows a homogenous film with some faint diffuse contrast stripes perhaps due to nano-pores or density variations running vertically. The structure of the specimen appears amorphous by electron diffraction (Fig. 3(b)) and atomic resolution imaging (Fig. 3(c)). From Table 1 we see that sample S3 was reactively sputtered with 3% flow percent oxygen which resulted in more than fifty percent oxygen in the film as seen from Table 2. It is fair to consider the film to be an oxide. We will comment on the check of the structure by XRD in Section 3.2 and discuss why it appears amorphous in Section 3.8.4.

Table 3
Atomic percentage of metal elements from STEM/EDS area scans.

Sample	Fe(at. %)	Co(at. %)	Ni(at. %)	Cu(at. %)	Ge(at. %)	Total(at. %)
SO	18	20	20	24	19	100
S3	19	16	15	27	23	100
S15	17	20	24	21	18	100

The uncertainty is around 5%. See Table 2 for oxygen concentration.

3.1.3. Sample S15 ASD

Fig. 4 shows cross-sectional STEM images of S15 ASD. It shows a homogenous film. In Fig. 4(a) is seen a faint columnar contrast along the growth direction. The specimen is nano-crystalline as can be inferred from the fringes in the high-resolution image of Fig. 4(b). That is in contrast to the structure of the specimen of S3 ASD, which appears amorphous by TEM (see Section 3.1.2). We will discuss the structural differences between S3 and S15 in Section 3.8.4. Here we just state that while FIB preparation can influence the specimen structure, the fact that the structure of S3 and S15 are different from each other after the FIB preparation, implies that the original film structure of S3 and S15 also are different from each other, when the FIB preparation process is identical. We will compare with XRD observations in Section 3.2. The results of electrical and optical properties are presented in Sections 3.6 and 3.7 respectively and will give further insight into differences between S3 and S15. We will conclude in Section 3.8.4 that all observations are consistent with S3 and S5 having a film structure as indicated in Table 2.

3.2. XRD

3.2.1. ASD samples

Fig. 5 shows XRD patterns obtained for the ASD samples S0, S3 and S15. There are no peaks in the diffractograms obtained for S3 and S15. Thus, those films appear as amorphous by XRD. However, for S0, there is one peak in the diffraction pattern (see Fig. 6 for a wider range). The peak position is at $2\theta = 43.54^\circ$ and the full width at half maximum width is $\sim 1^\circ$ This peak is assigned to the 111 reflection of an FCC structure

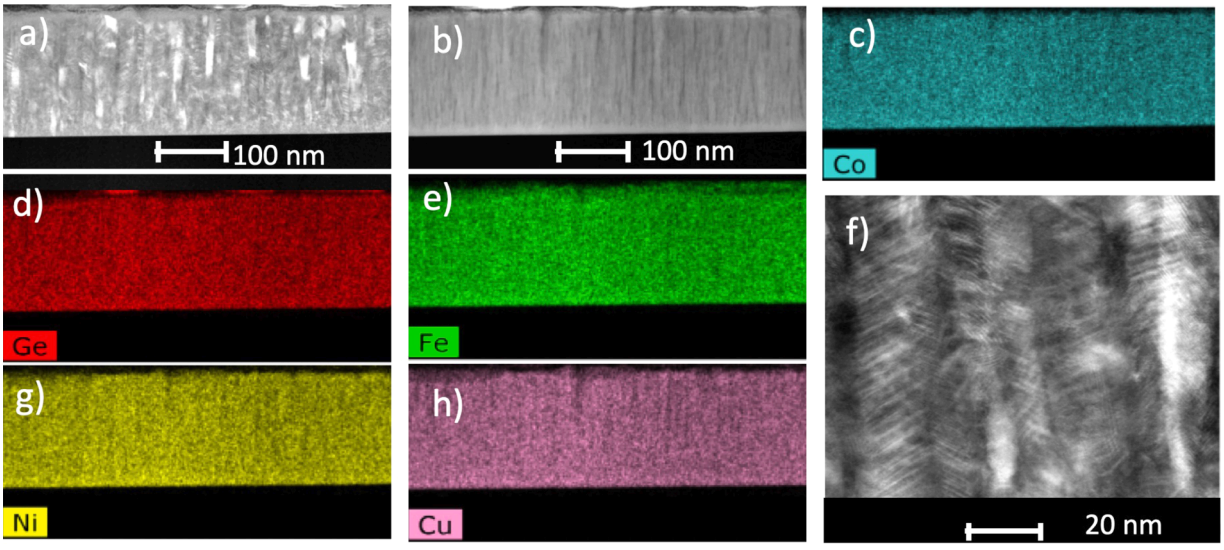

Fig. 1. TEM images of sample S0 ASD (sputter deposited FeCoNiCuGe film). All images have the sample surface on top, and all images, except f), have the same magnification and show the same area of the film with the interface to the silica substrate at the bottom. a) is a low-angle dark field image and b) is a high-angle dark field image. c),d),e),g) and h) show EDS element maps.(see Table 3 for quantifications) f) is a magnified detail showing columnar grains with a high density of planar defects.

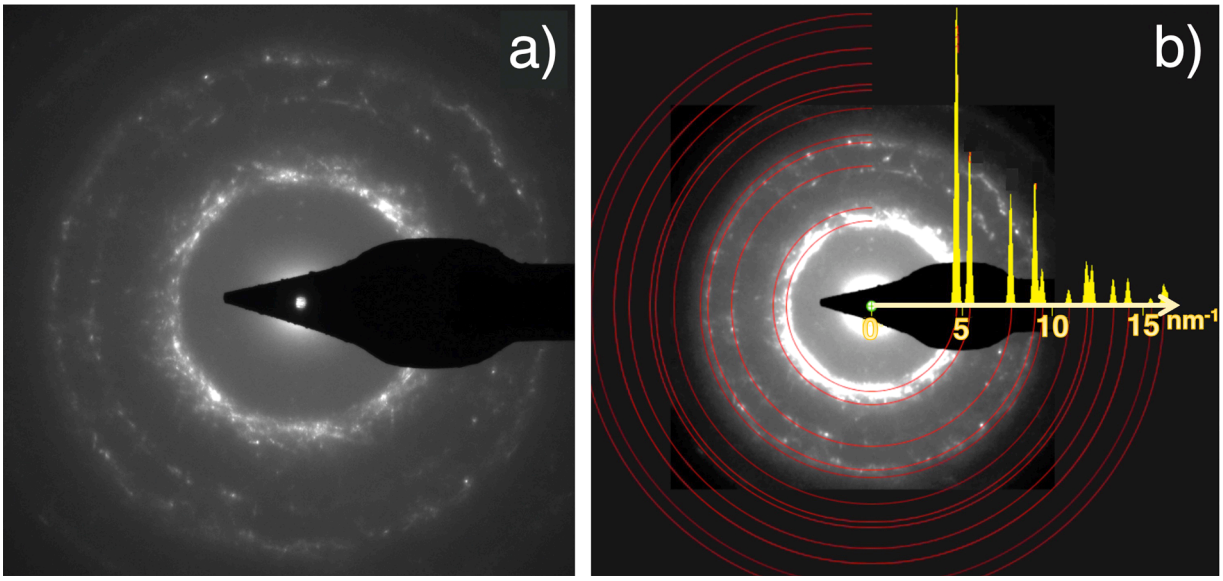

Fig. 2. SAD pattern of sample S0 ASD (same film as in Fig. 1) a) Experimental diffraction pattern. b) Calculated FCC ring pattern and intensity diagram superimposed on the experimental pattern.

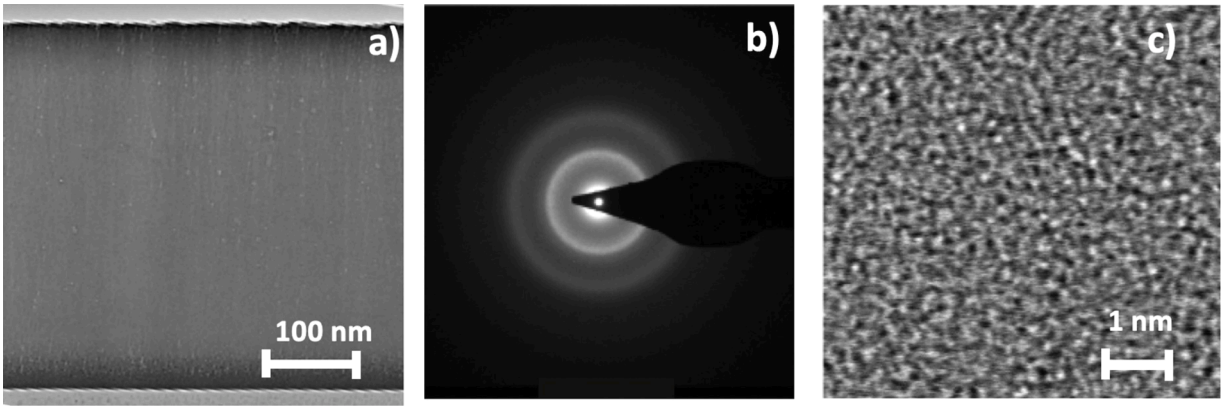

Fig. 3. STEM images of sample S3 ASD. a) is a cross sectional view with the substrate at the bottom. b) Is a diffraction patterns showing diffuse rings characteristic of amorphous material. c) High resolution image, showing no ordering of the atoms.

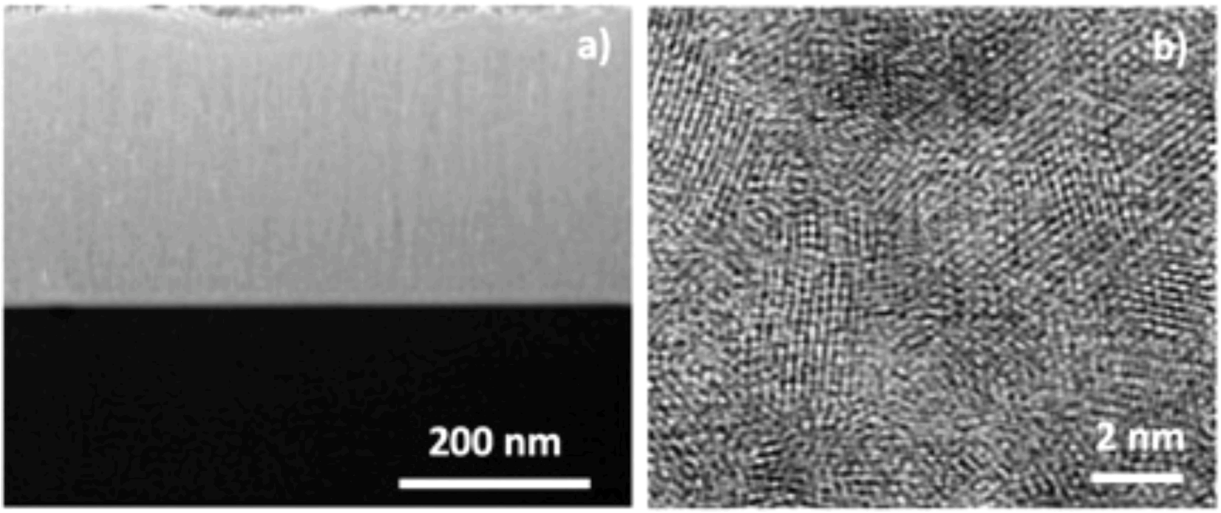

Fig. 4. Dark field STEM images of sample S15 ASD. a) cross sectional view with the substrate at the bottom. b) high-resolution image, showing lattice fringes of nanocrystallites. with size around 1–3 nm.

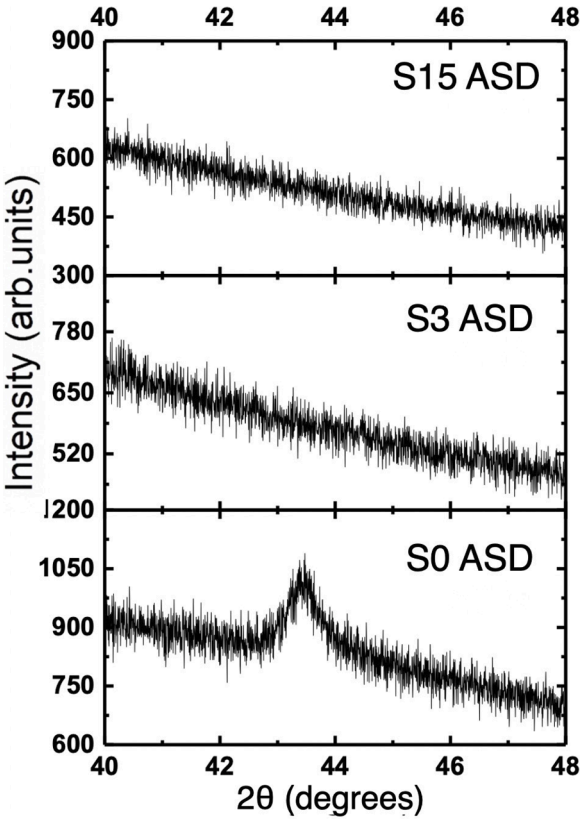

Fig. 5. XRD patterns of as-deposited films prepared with different O_2:Ar flow ratios. See Table 1 and Table 2 for details on samples S0, S3 and S15. See Fig. 6 for a wider range for S0.

(A1, $Fm\bar{3}m$, # 225). The large width can have contributions from coherency length limitations and micro-strain. Local strain from different atom sizes would contribute to reduction in intensity according to the analysis of Owen et al. [26]. The XRD analysis for S0 is then in agreement with the description of the TEM results given in Section 3.1.1 (Fig. 2). By assigning the peak to a 111 reflection from the FCC phase, the average atom radius derived from the XRD is 127.2 pm. The atom radius for the elements in their natural crystal structures are shown in Table 4. The mean of these is 124.9 pm. This mean value and the XRD value are reasonably similar. Considering that physical vapor deposited films commonly have some built-in stress[27, 28], and that S0 contains some amounts of oxygen, differences are expected. We will compare with other groups' results on related HEA systems in Section 3.8.2 and discuss how S0 fits into the HEA label in Section 3.8.3. That the S3 and S15 are XRD-wise like amorphous will be compared with the TEM results and discussed in Section 3.8.5.

3.2.2. *Annealing of S0 in O_2 and NMH*

The samples that were "XRD-amorphous" in the ASD condition, namely the reactively sputtered films with O_2, S3 and S15, remained "XRD-amorphous" after annealing in O_2 and thus the XRD showed no features. We thus only show the results for S0 which is the film sputtered with no oxygen. Fig. 6(a) shows the XRD patterns observed for S0 annealed in O_2 for 2 h at the temperatures annotated. It is seen that there are changes in the XRD patterns after each annealing temperature. The peak observed for the ASD case at 43.54° is attributed to the 111 reflection of a metal FCC structure. After the 300 °C anneal, this peak has disappeared and another peak is observed at 45.19 ° The position matches a 110 reflection of a metal BCC structure, indicating a phase transformation. After the 400 °C annealing, several peaks which could be associated with CuO appeared. There may also be 110 BCC reflections from metal alloys containing different concentrations of the elements. The peaks could also have contributions from $CoGeO_3$. After the 500 °C anneal, the peaks associated with oxides remain, while a new peak that appeared at 46.52 ° could not be identified. If this peak was hypothetically assigned to a 110 BCC metal reflection, it would have to correspond to a metal atom radius of 119.4 pm, which would be improbably small, considering Table 4, and ruling out that hypothetic assignment. We will present experimental data on SIMS measurements of the elemental distribution with depth in Section 3.3 indicating the segregation of Cu to the surface being oxidized.

3.2.3. *Annealing of S3 and S15 in NHM*

The samples were annealed in a flow of NHM for different reasons. Firstly, to test the assignments made in the XRD pattern of S0 annealed in O_2. Fig. 6(b) shows the diffraction patterns observed for sample S0 after annealing in the flow of NHM at the temperatures annotated. The observed evolution has many features in common with the patterns observed after annealing in O_2 flow, which may be surprising at first. It introduces some doubts about the above suggested XRD peak assignments made for S0 annealed in O_2. In particular, the XRD patterns after the 400 °C annealing is nearly identical for annealing in O_2 and for annealing in NHM. We would not expect oxides to appear as a result of annealing in NHM. That makes an argument for the phases present at 400 °C not being oxides, but unidentified multi-element intermetallic compounds. Alternatively, if the compounds observed after 400 °C annealing are oxides, then the oxygen in those oxides does mostly not originate from the annealing ambient, but from oxygen already being present in the ASD film, which here could be up to 10 percent (see Table 2), making it likely that oxides can grow and give diffraction. From Fig. 6(b) for the 500 °C annealing in NHM, it appears that the phases present and giving XRD peaks, are metal alloys with BCC structure of different compositions. The peaks being associated with oxides for the case of annealing in O_2 are not in the XRD and the unidentified peak indicated by "?" in Fig. 6(a) is not present. NMH is a reducing atmosphere so it is reasonable that oxides can be reduced, while it would not be expected that intermetallic compounds should disappear. This comparison between O_2 and NHM favors that the XRD peaks assigned to oxides in Fig. 6 are indeed from oxides, even if their exact identity is still uncertain.

The "oxide samples" S3 and S15 were annealed in NMH in order to check the stability of the oxide in that atmosphere. Fig. 7 shows the diffraction patterns observed for sample S3 and S15 after annealing at the temperatures indicated. It is seen in the figure that some diffraction peaks appear after annealing at 300 °C and the same peaks remain after 500 °C annealing. These match the presence of an FCC phase originating from a mixture of the metals present and for the S3 sample thee is a good match to hexagonal Ni_5Ge_3, while this intermetallic is not present in S15 after annealing. In S15 there is a match for the presence of a metallic FCC and BCC phase and hint of a spinel phase($Ni_xCo_{1-x}Fe_2O_4$)

3.3. *SIMS characterization of S0, ASD and 400 °C anneal in O_2*

Fig. 8 shows SIMS profile measurements on sample S0 by a cesium primary ion beam. The SIMS signal for each element is related to the concentration of the element and the sputter time is related to depth below the original surface. For S0 ASD it can be seen from Fig. 8(a) that the metals are distributed uniformly with depth. The sensitivity factor for each element has not been introduced in the figure, but the actual concentrations can be taken from Tables 2 and 3 within the uncertainties. The sputtering profile characteristics changed much after annealing the sample for 2 h at 400 °C in O_2 (see Fig. 8(b)). The ionization coefficient for each element changed between Fig. 8(a) and 8(b) because of a modified matrix for each element in the annealed sample, and we can only get qualitative information from the profiles. The qualitative distribution with depth is significant from Fig. 8(b). We can thus summarize the features that appear qualitatively valid for the

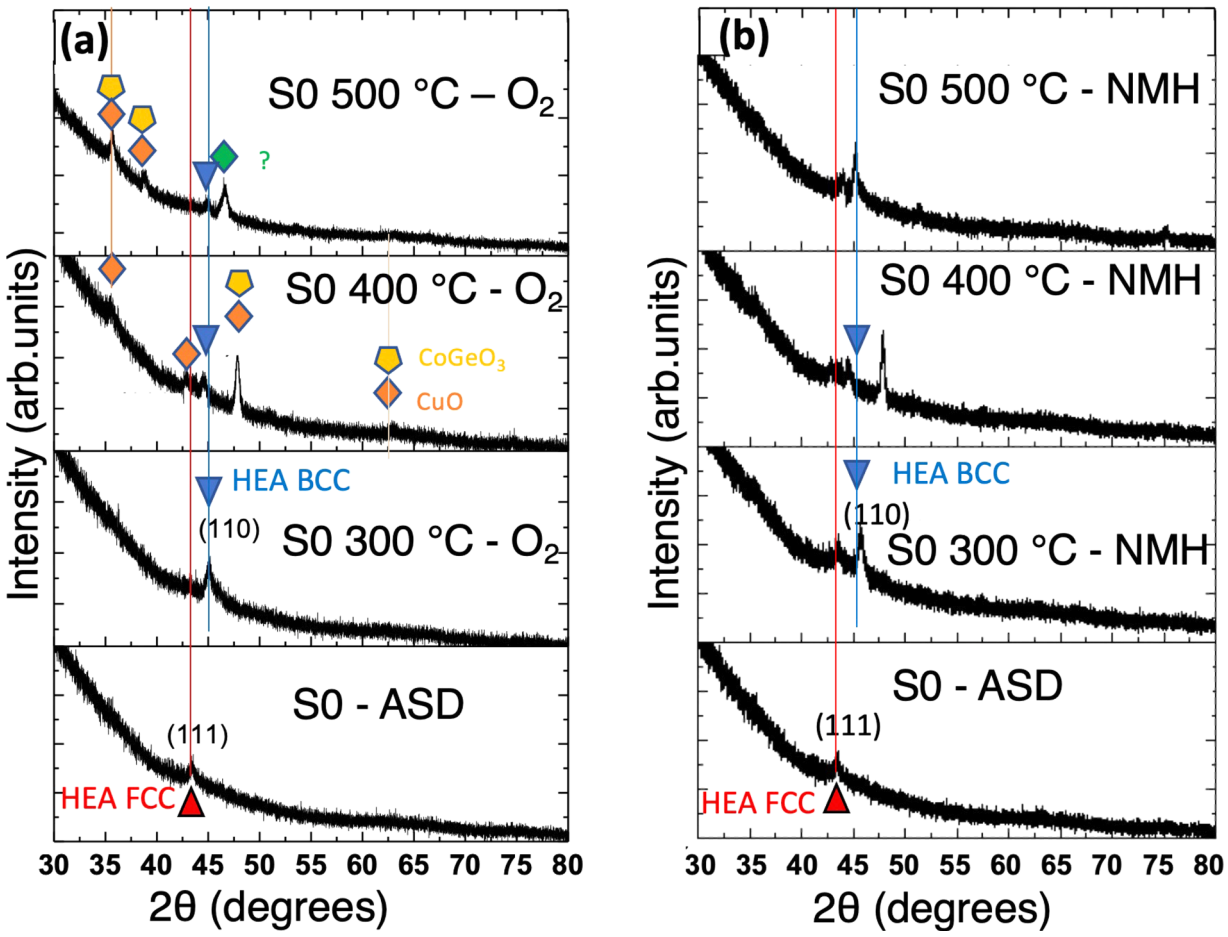

Fig. 6. XRD patterns of sputtered FeCoNiCuGe films SO as-deposited (ASD) and annealed after deposition to the temperatures indicated in (a) O_2 ambient. (b) Forming gas Nitrogen-Hydrogen-mixture. The patterns are collected at RT. The peaks have been marked with a matching identification.

Table 4
Crystal structures for the pure elements.

Element	Fe	Co	Ni	Cu	Ge
Crystal structure	BCC	HCP	FCC	FCC	diamond
Atomic radius (pm)	124.1	125.4	124.6	127.8	122.5

The atomic radius is calculated as half of the nearest neighbor distance in the respective crystal structure.

characteristics of Fig. 8(b) for sample S0 after heat treatment in O_2: (i) The elemental distribution with depth has changed much by the heat treatment. (ii) The most pronounced feature is the large redistribution of Cu. There is a large enhancement in a layer close to the surface. One should be cautious about surface artifacts in SIMS signals at the very surface; however, the region of Cu enrichment extends well into the bulk of the film. (iii) There appears to be an enhanced oxygen concentration in the surface region together with Cu.

3.4. SEM characterization

3.4.1. Sample S0 ASD and annealed in NHM

Fig. 9 shows SEM images of sample film S0. Fig. 9(a) and (b) show a homogenous smooth sputter deposited surface. After annealing for 2 h at 500 °C in NHM, precipitates are clearly visible as seen in Fig. 9(c) and (d). There are needle-like precipitates (Fig. 9(c)) and there are also areas that have small nanoparticles evenly distributed in a matrix (Fig. 9(d)). The structure of film S0 is not stable upon annealing. That was evidenced also by XRD shown in Fig. 6(b). The needle shaped nanostructures could originate from oxides. There are examples of nanowire synthesis of NiO [29], FeO [30], and CoO for supercapacitors [31].

3.4.2. Sample S3 annealed in NMH

It is seen from Fig. 10 that the S3 ASD sample is smooth with no apparent surface structure (see Fig. 10(a)). After annealing at 500 °C in NHM there is segregation of intermetallic compounds and metal alloys, and a very rough surface is visible. These were identified as the intermetallic Ni_5Ge_3 and a FCC metal alloy by XRD (Fig. 7(a)). In Section 3.6.7 we show that the S3 film after annealing in NHM at 500 °C has an overall electrical conductance like a metallic HEA, while like an oxide semiconductor before the annealing.

3.4.3. Sample S15 annealed in NMH

It is seen from Fig. 11(a) that the S15 ASD sample is smooth. However, after annealing at 500 °C in NHM the surface is rough with many cracks.

3.5. Summary of structure

The S0 ASD films have an FCC structure with near equiatomic composition, showing a texture with columnar grains containing many planar defects. The structure is unstable upon annealing in forming gas and showed demixing. Annealing in O_2 also yielded inhomogeneous oxides, with a thick layer of CuO growing on the surface. The as-deposited S3 and S15 are oxide films that are amorphous and nanocrystalline respectively (see Table 1 and Table 2 for some of the

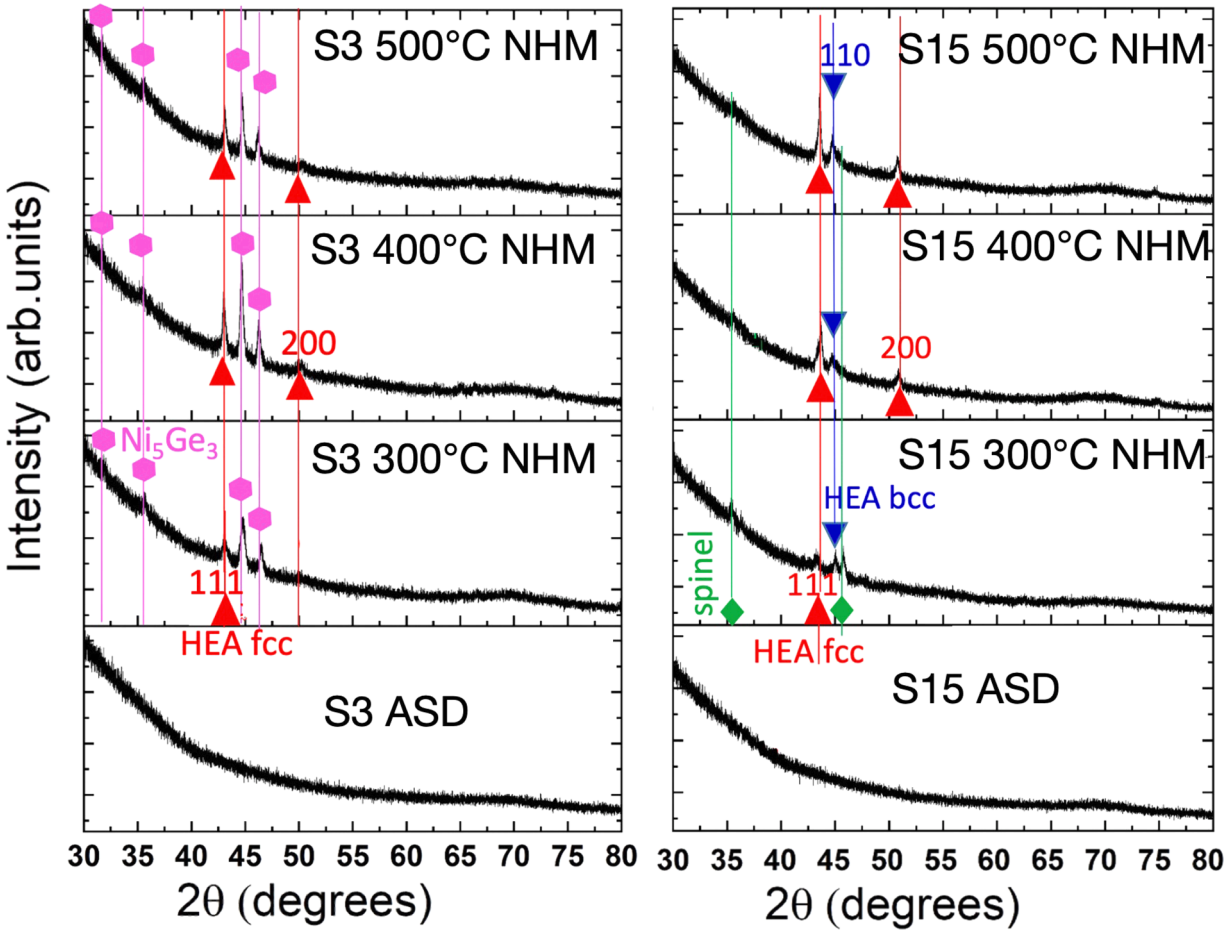

Fig. 7. XRD patterns of samples S3 and S15 annealed in an ambient of Nitrogen Hydrogen Mixture (NHM) at temperatures indicated. The origins of the peaks have been suggested. In S3 some amount of FCC structure may appear together with hexagonal Ni_5Ge_3. In the S15 sample a HEA FCC phase and a HEA BCC phase appears. It is also possible some spinel phase of the type $Ni_xCo_{1-x}Fe_2O_4$ occur in the samples with peaks overlapping that of other phases.

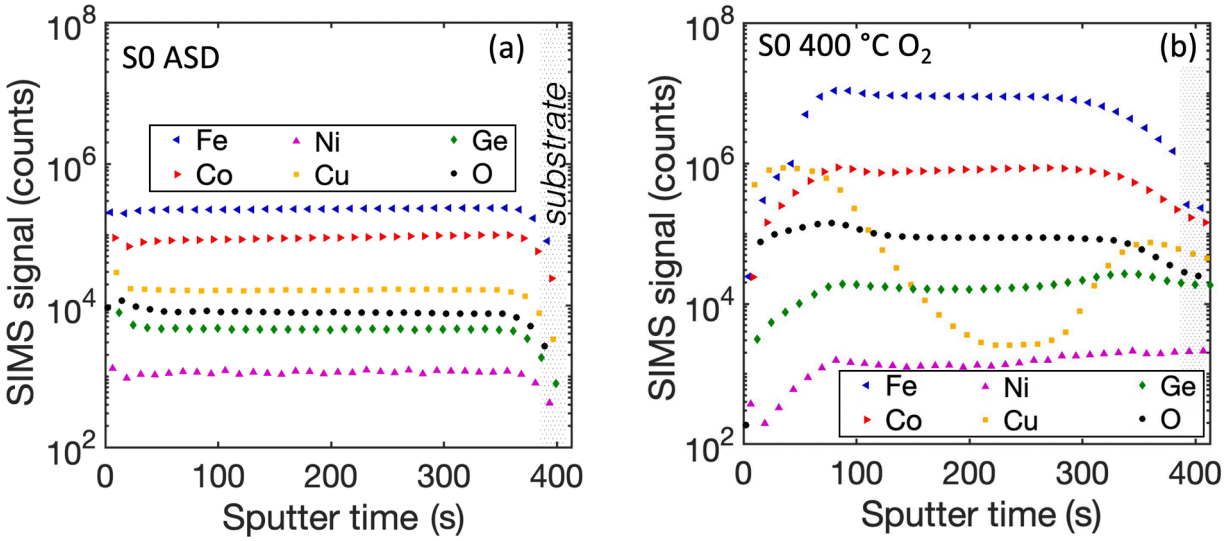

Fig. 8. SIMS profile showing the distribution of the elements in the film with depth from the surface(on the left) towards the substrate (on the right). (a) The film S0 as-deposited. The distribution of the elements appears uniform with depth. The region closes to the substrate may have ionization artifacts and should be ignored. (b) The same film S0 after annealing at 400 °C in O_2 for 2 h. It is seen that the element distributions have changed and vary much with depth.

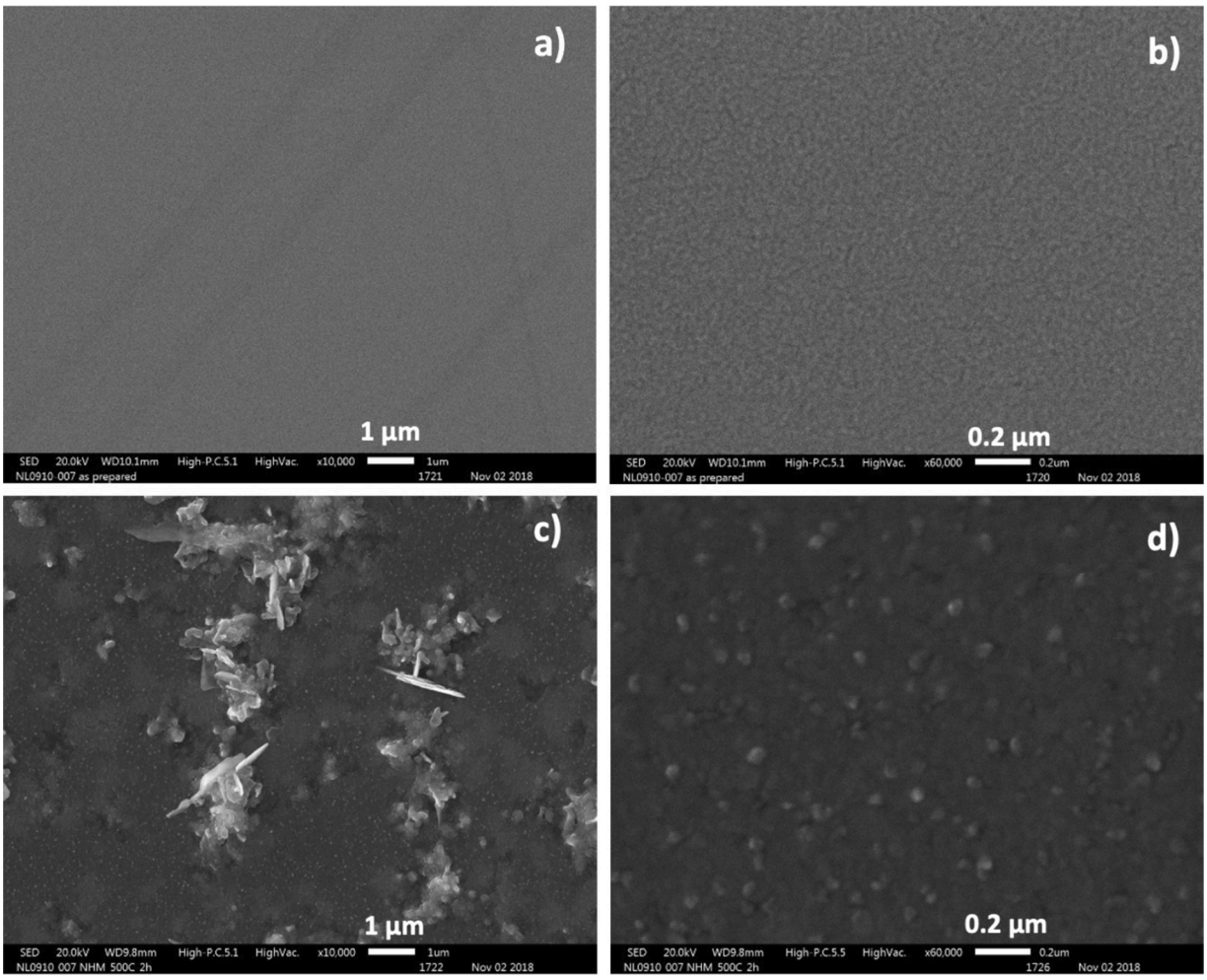

Fig. 9. SEM images of the surface of sample S0. a) and b)The as deposited film. c) and d) annealed for 2 h at 500 °C in NHM.

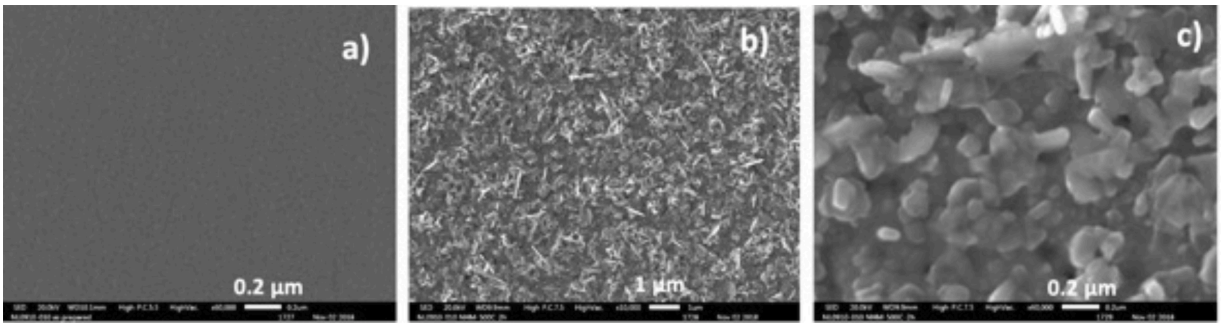

Fig. 10. SEM images of sample S3. a) as deposited b) after annealing in forming gas at 500 °C. c) Also after 500 °C annealing, but higher magnification.

conditions and measured parameters).

3.6. Electrical properties

3.6.1. Resistivity of ASD films

The temperature dependence of the resistivity gives information on the electronic structure. Fig. 9 shows the measured resistivity of S0 and S3, both in ASD condition, as a function of measurement temperature compared to the resistivity of crystalline Cu. Notice that the resistivity of S3 is 18 orders of magnitude higher than that of Cu at low temperature. The resistance of S15 was too large to be measured on the available measurement setups. That could be due to a combination of high resistivity and high contact resistivity. There is also a large difference in the resistivity and temperature dependence of S0 and S3. We describe the S0 characteristics first.

3.6.2. Discussion of temperature dependent resistivity of S0 ASD

It is seen that the relative change in resistivity of S0 ASD with temperature is small, the curve for S0 in Fig. 12(a) appears flat, so that the most important contribution to the resistivity can be described as residual resistivity, ρ_i, that is temperature independent and attributed to alloy scattering arising due to chemical site disorder. Scattering from impurities such as oxygen atoms would also contribute to ρ_i The residual resistance ratio is equal to: RRR = ρ(RT)/ρ(20 K) = 1.12. The film has a

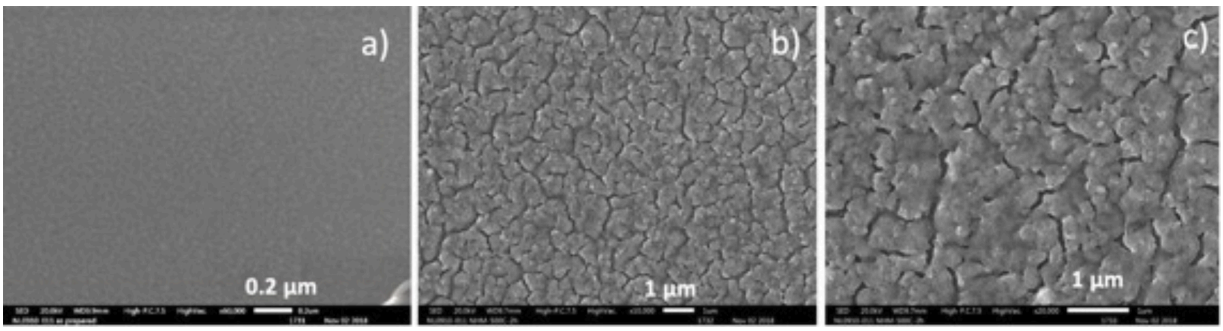

Fig. 11. SEM images of sample S15. a) as deposited b) after annealing in forming gas at 500 °C. c) also after 500 °C annealing, but higher magnification.

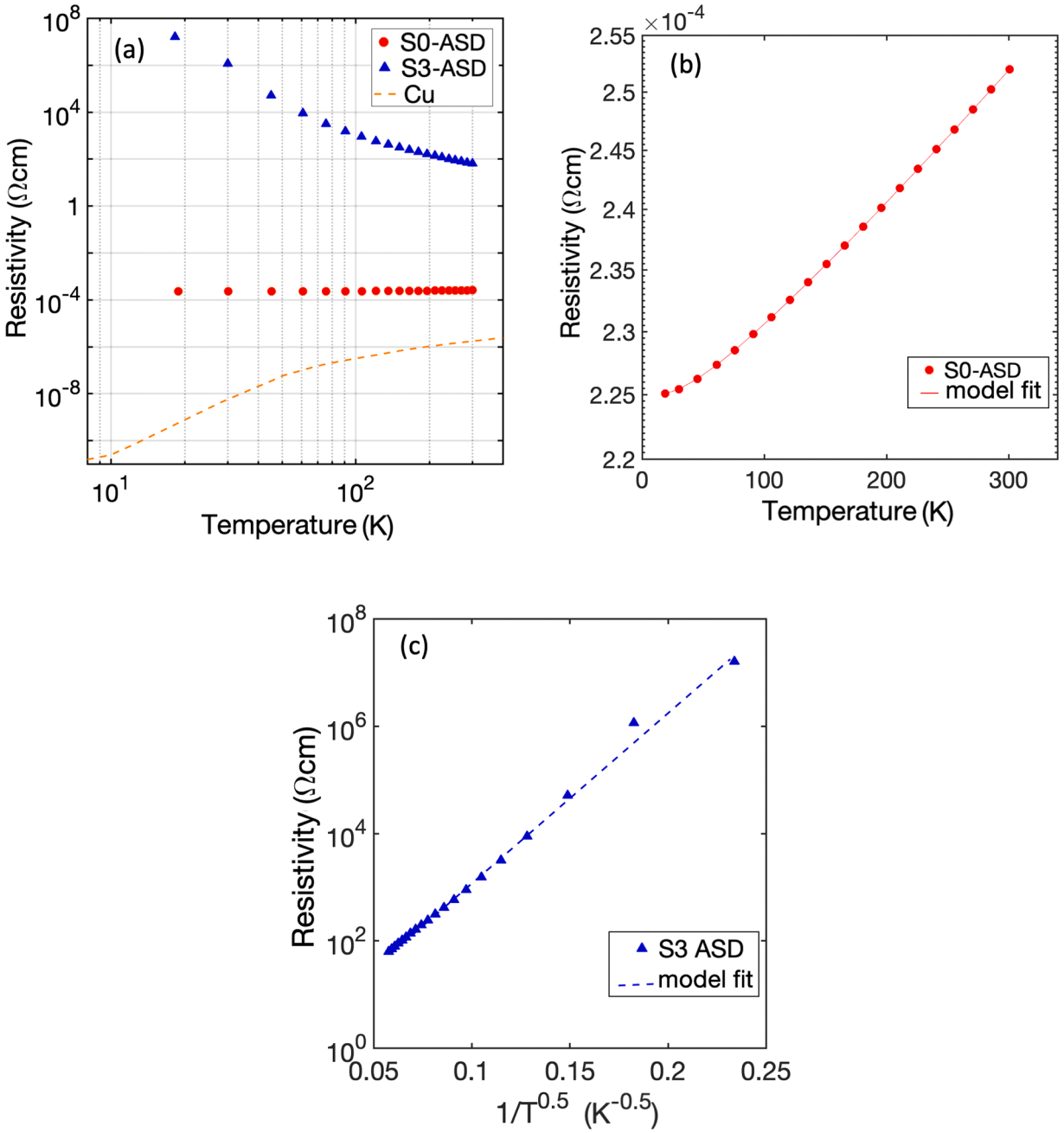

Fig. 12. Resistivity of samples measured as a function of measurement temperature. (a) Resistivity of S0 and S3 in log scale compared to that of Cu. (b) Expanded view of the resistivity of S0 showing a steady increase approaching linear dependence. The line is a model fit(see Section 3.6.2). (c) Resistivity of sample S3 plotted as a function of $1/T^{0.5}$. The dashed line is a fit to Efros–Shklovskii theory (see Section 3.6.4).

small temperature coefficient of resistance (TCR = $\partial\ln(\rho)/\partial T$) that is smaller than 4.5 ppm/K over the whole temperature range. Similar, but even smaller TCR's have been observed for other HEA's. For CrFeCoNiCu sputtered films it has been observed 1.04 and 2 ppm/K, respectively, for RRR and TCR, respectively [32]. The shape of the temperature variation of the resistivity of S0 ASD is seen more clearly in Fig. 12(b). It is seen that the resistivity is increasing with temperature. A common definition of a metal is a material whose resistivity increases with temperature [33]. It is thus natural to categorize S0 as metallic, also since the optical reflection is metal-like and the film absorbs completely between 300 and 2500 nm as presented in Section 3.7(see Fig. 18(a)).

For an idealized textbook metal, the electrons experience a periodic potential giving that the electrons are described by Bloch states. The resistance of a metal originates from breaking the periodicity. Lattice vibrations and impurities are the main contributions. For the HEA one also has deviations from periodicity due to that the random distribution of the elements on the lattice sites. In addition, there is the local distortion due to atomic size mismatch [34]. XRD gives information on these distortions via scattering of X-ray scattering [26], and resistivity measurements give information via electron scattering. Neither result is straight forward to analyze though. For the resistivity of S0 ASD we can for the discussion describe the resistivity as a large temperature independent resistivity, ρ_i plus a temperature dependent term that increases steadily with temperature.

$$\rho(T) = \rho_i + \rho_{BG}(T) \tag{1}$$

If we consider the temperature dependent part only, it has many characteristics quantitatively in common with the resistivity of elemental metals and for S0 SD it can even be fitted to the common Bloch-Grüneisen expression [35],

$$\rho_{BG}(T) = 4.226259\rho_{\theta_E}\left(\frac{T}{\Theta_R}\right)^5\left(\int_0^{\frac{\Theta_R}{T}}\frac{x^5}{(e^x-1)(1-e^{-x})}\mathrm{d}x\right) \tag{2}$$

for the resistivity with parameters Θ_R=315 K and $\rho_{\theta_R} = 2.46\times10^{-5}$ Ωcm being the Debye temperature of resistivity and the resistivity at that temperature respectively. These parameter values are in the range of the parameters for common metals, further exemplifying the similarity to metals. However, when we consider the magnitude of the total resistivity, we realize it is larger than the Mott [36], or Mott -Ioffe-Regel (MIR) limit [37] which is ρ_{max}≈100 μΩcm. The observation of resistivities higher than the MIR limit is sometimes taken as an indication that the transport is not governed by quasiparticle transport, i.e., not described by Bloch states and the theories using that assumption, such as the Boltzmann transport equation, and certainly the Bloch-Grüneisen expression. However, the fact that the temperature dependence of the resistivity has close similarity to metals indicates that the energy dissipation has much in common even if the quantum mechanical description cannot be the same. It should also be commented that a resistivity at the MIR limit imply an equivalent effective mean free path of the order of interatomic distances. Then the special scattering mechanisms typical for thin films such as surface scattering and grain-boundary scattering do not have a dominant role.

It could also be noticed that for S0 ASD there is no negative slope for the resistivity at the lowest temperatures, while there is a negative slope for sputtered CrFeCoNiCu HEA films [32], even if the actual resistivity is highest for S0. A negative slope at low temperature is sometimes associated with weak localization. It is believed that weak localization effects in combination with negligible electron–phonon coupling are responsible for negative TCRs in metals [38]. It has been shown that weak localization suppresses the electron-phonon interaction [39]. The absence of negative TCR could then indicate that the electron-phonon interaction is stronger for FeCoNiCuGe than for CrFeCoNiCu. Another reason for the difference between CrFeCoNiCu and FeCoNiCuGe could be in their magnetic properties and be related to Cr which would promote antimagnetic coupling between Co, Ni and Fe, and not promote paramagnetic domains. This could yield conditions showing Kondo effect [40]. More detailed experiments on magnetic properties would be required to test this.

3.6.3. Electrical characteristics of annealed S0 samples

We observed from XRD (Fig. 6(b) and SEM (Fig. 9) that S0 is not stable upon annealing. This is also reflected by changes in the resistivity for annealed samples as seen in Fig. 13. After annealing at 400 °C for 2 h in NHM the resistivity dropped to 40% of its ASD value, and the value then dropped further by about 1% for annealing to 500 °C. Since the structural changes observed with annealing implies phase separation, the measured resistivity of the film should be regarded as an effective medium property. We observed by XRD that both the FCC and BCC phase was present after annealing even at 300 °C for 2 h and it is natural that these phases have somewhat different compositions. These regions of different phase and composition will then have less disorder, yielding less alloy scattering than the ASD sample, and the heat treatment could also anneal out some defects. The latter may include segregation of oxygen. We will then have conduction in an effective medium with phases of higher order than the ASD case which results in higher conduction. Unfortunately, the films also decompose more severely at higher temperatures with rod-like structures forming seen in Fig. 9. Further work is required to understand these structures in detail.

3.6.4. Temperature dependent resistivity S3 asd

Here we comment on the temperature dependence of resistivity for S3 ASD as seen in Fig. 12(c). We see that the TCR is negative at all temperatures, and its absolute value is very large compared to that for S0. These are typical characteristics for semiconductors. We have initially tested if the temperature dependence could be described by a simple Boltzmann factor $\rho=\rho_0\cdot\exp(\delta_E/kT)$ with a simple activation energy δ_E. It was clear that the dependence was far from that with a single activation energy. The data could be fit with that functional form only over very small temperature intervals, and with a δ_E which was different for each interval and very small <0.01 eV at the lowest temperature. Sometimes a distribution of activation energies can result in an expression for the resistivity like: [41]

$$\rho(T) = \rho_0 exp\left(\left(\frac{\Delta E}{kT}\right)^{\beta}\right) \tag{3}$$

where the value of β can vary between 0.1 to 2, and ΔE is a characteristic energy of the distribution, k is the Boltzmann constant and T is the absolute temperature. Eq(3) also describes variable range hopping when

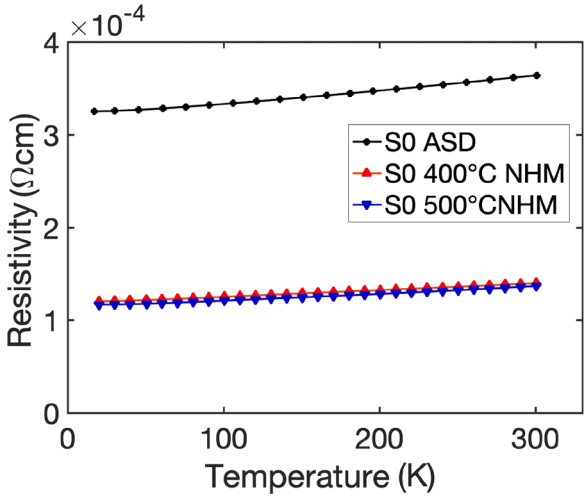

Fig. 13. Resistivity as function of measurement temperature for sample S0 ASD and after annealing in NHM at the temperatures indicated.

the problem is treated as hopping between quantum states having a distribution in energy and position. The famous mathematical treatment of Mott [42] gave $\beta = 1/3$, while the Efros–Shklovskii theory [43] of variable range hopping including Coulomb repulsion between carriers yielded $\beta = 1/2$. In Fig. 12(c) we plot the resistivity in a log scale and $1/T^{0.5}$ as the abscissa. It is seen that the behavior fits the Efros–Shklovskii theory [43] for hopping conduction describing conduction via a tail of localized states below the conduction band of an amorphous semiconductor. Localized states above the valence band gives the same result.

3.6.5. Seebeck coefficient of S0 asd

Here we comment on the measurements of the Seebeck coefficient for S0. It is shown in Fig. 14(a) as a function of temperature. We want to focus on the sign of the Seebeck coefficient. It is clearly negative over the temperature range. Often the Seebeck measurement is used to indicate the carrier type of a material. So, from only this measurement one would suggest that the dominant carriers are electrons. The measurement points of Fig. 14(a) are connected with lines indicating measurements during heating up and cooling down respectively. The slight difference can in general be due to structural changes in the sample induced by the temperature and measurement artifacts due to possible different temperature distribution in heating up and cooling down. We ignore this in our further discussion, we only emphasize that the Seebeck coefficient is negative. However, the Hall coefficient seen in Fig. 14(b) is positive in its temperature range. The Hall coefficient is also often used to find the carrier type of a material, and it gives that holes are the dominant carriers. There is no conflict in that the Seebeck coefficient and the Hall factor have different signs at room temperature where the measurements can be compared. We forward the hypothesis that both electrons and holes contribute to the conductivity in the material. We will check this hypothesis below by looking at the band diagram around the Fermi level. Both carriers will contribute, but the Seebeck coefficient and the Hall coefficient are weighted with different parameters. To illustrate that, consider the simplified case that we have only one band/kind of electrons and one kind of holes. Then the Seebeck coefficient α and the Hall coefficient R_H is given by [44]

$$\alpha = \frac{\alpha_p - \frac{\mu_n n|\alpha_n|}{\mu_p p}}{1 - \frac{\mu_n n}{\mu_p p}} \tag{4}$$

$$R_H = \frac{r\left(p\mu_p^2 - n\mu_n^2\right)}{q\left(n\mu_n - p\mu_p\right)^2} \tag{5}$$

where n, μ_n and α_n are the concentration, mobility and Seebeck coefficient respectively and p, μ_p and α_p are those for the holes. The symbol r is the Hall factor which has a value of the order of one and can be ignored in the current context. Both α and R_H will change sign when going from only holes to only electrons, but they change sign at different carrier concentrations. Thus, they can have different sign for a certain range of concentrations. We will see in Section 3.6.6 that having both electrons and holes is a reasonable hypothesis for the current case.

3.6.6. Computational evaluation of band structure FeCoNiCuGe

Ab initio calculations were performed with the Vienna Ab initio Simulation Package [45], employing the projector-augmented wave method [46] within the generalized gradient approximation of the exchange-correlation functional as determined by Perdew, Burke, and Ernzerhof [47]. Collinear spin polarization is enabled in all calculations. A cut-off energy of 550 eV is used, and the Methfessel-Paxton smearing method is applied with the parameter "SIGMA" equal to 0.2 in all density-functional-theory (DFT) calculations. These settings combined with the gamma-centered k-mesh of 4 × 4 × 4 guarantees total energy convergence within 1 meV/atom. In the present study, all alloy supercells are special quasi-random structures (SQS) [48] generated by the "mcsqs" code of the Alloy Theoretic Automated Toolkit package [49]. SQS is the best periodic supercell approximations to the true disordered state for a given number of atoms per supercell. The method is based on a Monte Carlo simulated annealing loop with an objective function that seeks to perfectly match the maximum number of correlation functions. This method optimizes the shape of the supercell jointly with the occupation of the atomic sites, thus ensuring that the configurational space searched is exhaustive and not biased by a pre-specified supercell shape. The optioned cell is fully relaxed with a free cell volume and free atomic positions. The optimized simulated FeCoNiCuGe cell is presented in Fig. 15 put together by joining supercells.

Fig. 16 shows the calculated band diagram of FeCoNiCuGe which represents sample S0. It is seen that there are many bands that cross the Fermi level, in particular those bands having pockets/regions around the Fermi level will be states contributing to conduction. We can identify pockets/regions with a positive effective mass as well as pockets/regions with a negative effective mass, corresponding to regions with electrons and holes respectively at the Fermi level. So, the calculations are in agreement with the hypothesis that both electrons and holes contribute to the conduction.

3.6.7. Temperature dependent resistivity S3 annealed in NHM

It is seen from insert in Fig. 17 that the resistivity of S3 is reduced

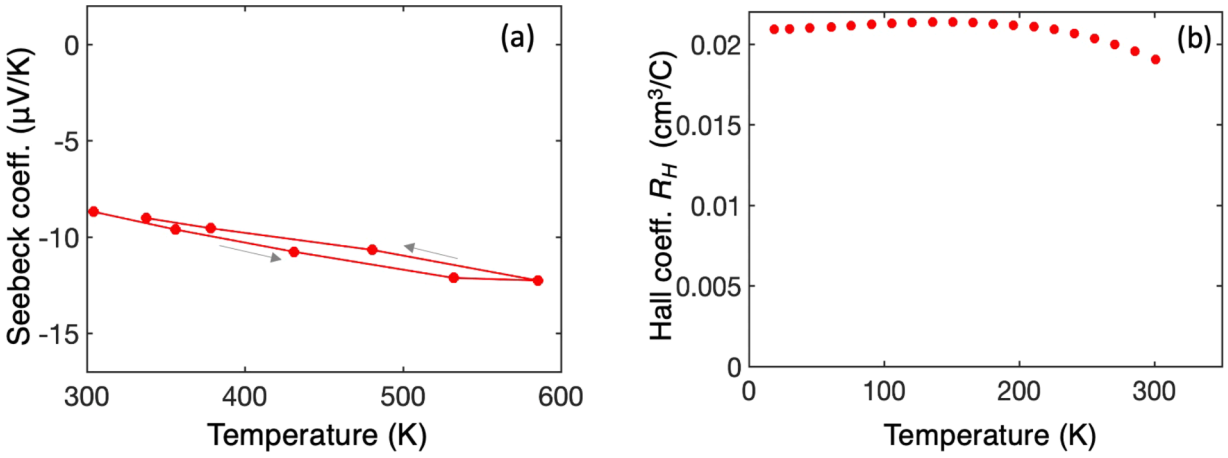

Fig. 14. Measurement related to the carrier type in sample S0 ASD. (a) The Seebeck coefficient. Notice that it is negative for all measurements. The arrows on the two curves indicate the time order of measurement for starting at high and low temperature respectively. (b) The Hall coefficient, RH. Notice that it is positive for all temperatures.

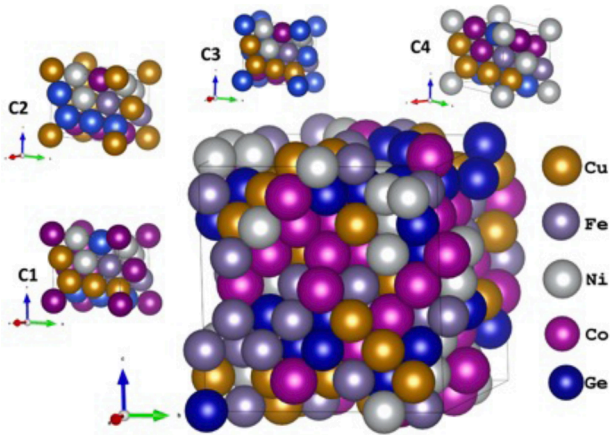

Fig. 15. Optimized cell used to represent FeCoNiCuGe. It has been put together by FCC fragments like C1, C2, C3 and C4. The special quasi random structure is used in DFT calculations of electronic structure.

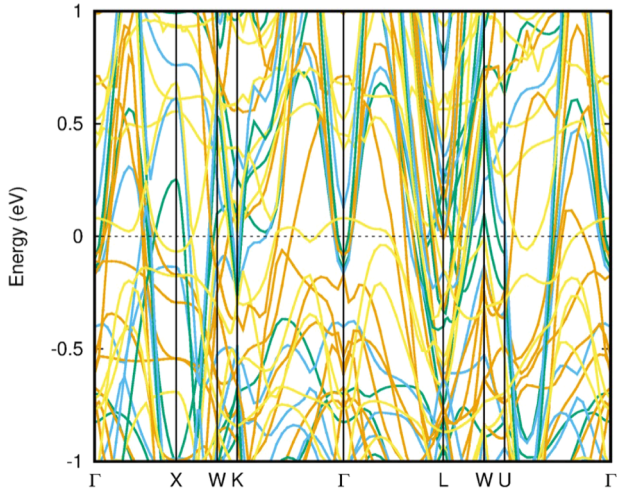

Fig. 16. DFT calculated band structure of FeCoNiCuGe near the Fermi-level. Notice that around the Fermi level there are band segments that have negative curvature as well as segments with positive curvature around the Fermi level, indicating that both electrons and holes contribute to the charge conduction.

many orders of magnitude by annealing in NHM. The annealing reduces the oxide and HEA metal phase and intermetallic compounds are formed. However, the film also becomes nonuniform. We have an effective medium with an effective resistivity. It is seen from Fig. 17 that the TCR also becomes positive by the annealing, so the dominating conduction is metallic-like after the annealing.

3.7. Optical transmission measurements

Fig. 18(a) shows the optical transmission of the ASD films in the wavelength range 300 −2500 nm. Sample S0 shows no transmission. It also looks metallic to the eye and the transmission is like that for a metal. The transmittances for the films S3 and S15 are quite different than that for S0. The curve for S3 and S15 have considerable transmission at longer wavelengths, and the shapes have similarities to those for semiconductor or insulator films. There is a strong increase in transmission from 500 −650 nm. The waviness is typical for thin film interference [50, 51]. We also show the absorption data plotted as a Tauc-plot in Fig. 18(b) where both samples S3 and S15 follow a Tauc-model for a material with an indirect bandgap around 1.9 eV. We discuss how the transmission measurements ties to the structural characteristics,

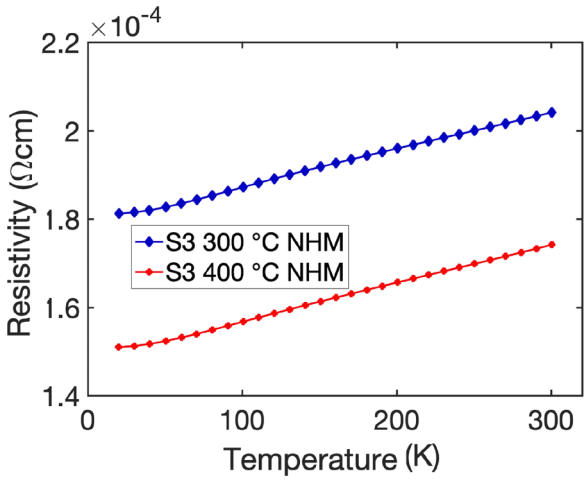

Fig. 17. Resistivity of sample S3 annealed in NHM at the temperature indicated. See Fig. 12(a) for the ASD case. For the annealed cases the film is inhomogeneous and the resistivity values should be treated as for an effective medium.

electrical characteristics, and compare with the reported oxides of the elements in Section 3.8.6.

The optical transmission of the samples has also been measured after annealing for 2 h at 300, 400 and 500 °C in O_2 ambient and the change in the transmission with annealing temperature is shown in Fig. 19(a) and (b) for sample S3 and S15, respectively. Sample S0 remained non transmitting after these annealing treatments (not shown). It is seen from Fig. 19(a) that for S3, the different annealing temperatures resulted in nearly the same change from the ASD case. The appearance of the curves for the annealed cases can be described as arising by a slight compression of the curves for ASD along the wavelength axis. It could correspond to a small change in the refractive index. The change in the fitted indirect band gap is small, if any (increases less than 0.1 eV). For the S15 sample the changes upon annealing are similar but, in addition, there is an increase in transmission for all annealing temperatures, in agreement with weaker absorption. We discuss how this annealing effect may be related to electronic structure in section 3.8.6.

3.8. Summary of results and their discussion

3.8.1. On the grainsize in S0 ASD

The (columnar) grain sizes observed for S0 ASD (see Fig. 1) is in the range 10–20 nm. For films grown by physical vapor deposition the grain size depends strongly on the diffusivity of the ad atoms [28]. The surface diffusivity may be the most important, but that usually scales with the bulk diffusivity. This dependence of diffusivity has made it possibly to develop models where the grain growth behavior of a film can be scaled by the melting temperature which again scales with the diffusivity [27, 28,52]. In part of the HEA literature, there has been an apparent faith in the myth that sluggish diffusion is a universal phenomenon laying behind the attractive properties found. If the sluggish diffusion had been a pronounced universal property of high entropy alloys one would expect that the grain sizes for S0 would be much smaller than those from metal films from the elements deposited under similar conditions. That is not the case. For example, for similar deposition conditions Anderoglu et al. [53] reported around 40 nm grain size for Cu deposited films, Vetterick et al. [54] reported around 35 nm for Fe and Neerinck et al. [55] reported 10 nm in-plane for $Ni_{0.8}Fe_{0.2}$ films. There is of course a distribution in size as well as a variation with the process parameters, but the universality of a large effect seems disproved when these examples are considered reliable. This is further strengthened by the detailed study of grain size versus thickness for Cu and for the HEA CrFeCoNiCu made by Dulmaa et al. [56] where the difference in size was

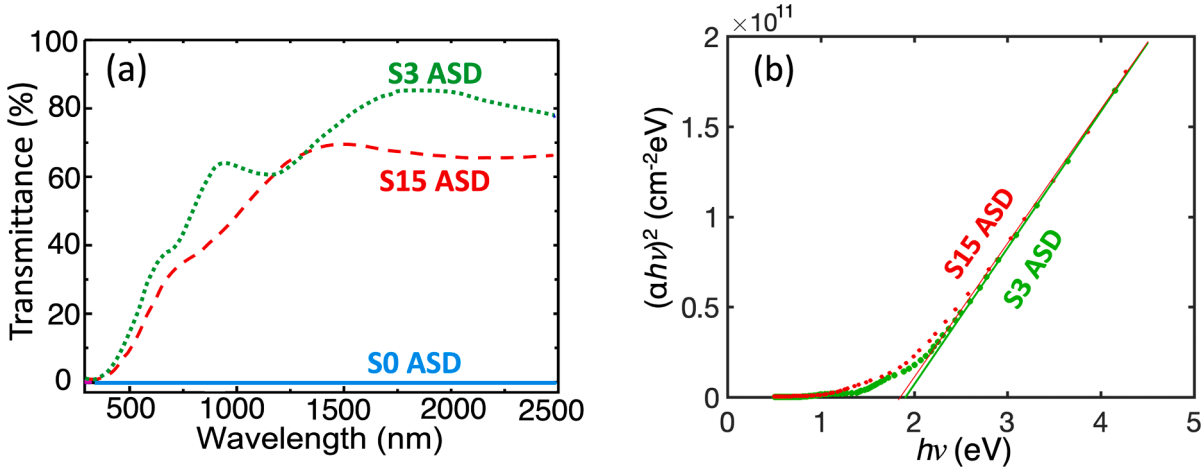

Fig. 18. (a) Transmission spectra of magnetron sputtered films using different O_2 flow rates represented by sample S0, S3 and S15. See Table 1 and Table 2 for the different parameters for the samples. Sample S0 appears metallic while S3 and S15 appears as semiconductors or insulators. (b) The data for S3 and S15 plotted as a Tauc-plot for indirect transitions.

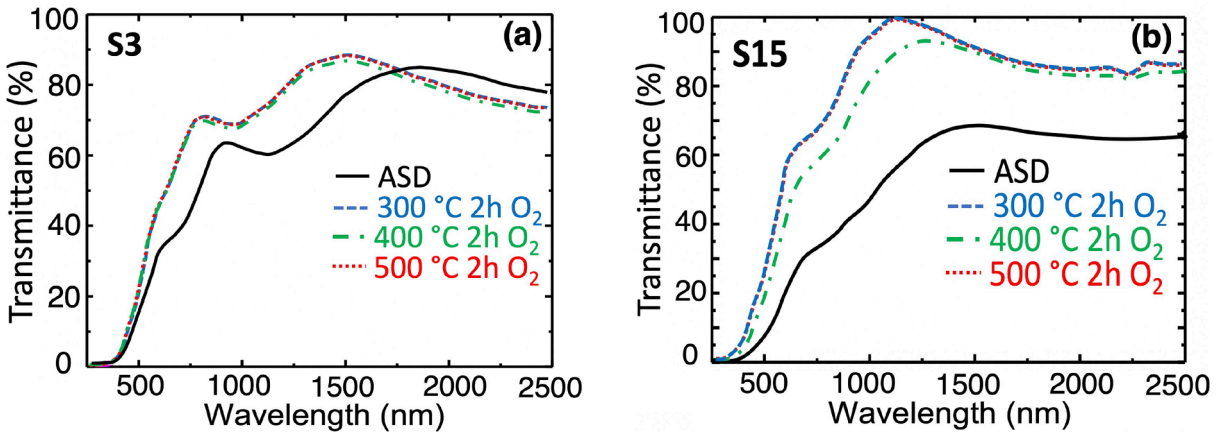

Fig. 19. Transmission spectra of samples as-deposited (ASD) and annealed in O_2 flow for 2 h at the temperatures indicated. (a) for sample S3. (b) for sample S15. See Table 1 and Table 2 for details on the samples.

only around 30%. It has been stated that the diffusion in HEAs is sluggish due to the local associated lattice distortion [34]. The effect on surface structure and surface diffusion is not well known for HEAs, but it is timely to note that recently several investigations that address diffusion have concluded that the diffusion is not sluggish for the HEA that have been carefully examined [57].

3.8.2. S0, comparison with other studies on CrFeCoNi and CrFeCoNiCu w. Ge

Even though no other reports could be found in the literature on the present system, we compare to a study having much in common: Vida et al. [58] studied the effect of adding Ge to a CrFeCoNi based alloy for bulk samples made by induction melting of the constituents. They reported on structure and hardness of the samples and found that the material had a two-phase structure; an FCC HEA phase and a BCC HEA phase with slightly different compositions. They correlated this with rules of thumb related to the valence electron count.

The XRD for S0 ASD (see Fig. 6) has resemblance to the XRD Braeckman et al. [20] observed for sputtered films of $CoCrCuFeNiGe_x$ for $x = 0.047$. They observed a pattern with several reflections for $x = 0$, but only the 111 reflection for $x > 0$ and at a considerable reduction of intensity. They suggest this could indicate that for low x, part of the film exhibits an amorphous phase. Although for different sputtering conditions, we also observe strong 111 reflections for $x = 0$ [32], but only weaker 111 when Cr is replaced with Ge as in S0, and that film does not contain amorphous regions. We suggest the low intensity 111 for S0 has to do with local strain from different atom sizes.

3.8.3. HEA aspects of S0

If one considers a HEA system to be stabilized by configurational entropy one would expect that the structure is stable upon heating to a high temperature where the entropy contribution to the free energy is largest. It is unknown whether a bulk system consisting of the elements of S0 will show a single FCC phase at high temperature. The thin film sample S0 shows a single FCC phase in the ASD state.(see Section 3.1.1) It can be questioned whether HEA is an appropriate designation for the present case of the thin films S0. The FCC structure and some of the features observed appear in line with the trends reported for material systems where the stabilization is attributed to high entropy. In the present work the film S0 is produced under non-equilibrium conditions. It is possible to view the sputter process as a case where the system consisting of adatoms in the sputter process has the possibility to run through many configurations because of the excess kinetic energy and also because of the smaller activation energy for diffusion of surface atoms compared to that of atoms in the bulk. Thus, each newly arrived adatom with excess kinetic energy is effectively experiencing a high temperature which is followed by a cooling process because of the fast dissipation of excess energy. The state with an initial high kinetic energy

is then frozen-in. Which configuration that state has is heavily influenced by entropy. A high entropy state is the configuration that occurs randomly most often, when the system runs through many configurations.

A HEA system that is stabilized by entropy at high temperature may become metastable at lower temperatures. That the ASD state is metastable at RT is evidenced by the change in structure when the film is annealed. (see Section 3.2.2, Fig. 6(b)) The most pronounced change is the separation into FCC and BCC phases upon annealing. Thus, it seems natural that the ASD state of S0 to be considered as a HEA. It may be interesting to compare the phase transition in these multi-element systems with the molecular dynamics simulations of phase transitions between BCC and FCC structures [59].

3.8.4. Discussion on the structure of S3 and S15

The STEM specimens for S3 and S15 were amorphous and nanocrystalline respectively (see Section 3.1.2 and 3.1.3 respectively). This indicated that the film structures were different too. That is consistent with the electrical properties of S3 and S15 being very different from each other (see Section 3.6.1) and that the annealing behavior of S3 and S15 are different from each other (see Fig. 7 for structural differences by XRD, see Fig. 10 and Fig. 11, for structural differences by SEM). Regarding the possible influence of FIB preparation on the structure STEM specimens, it is well known that FIB can influence the structure, for example creating an amorphous zone in the material. That is the most likely effect that could hypothetically occur and then obscure the true phase identification of S3, so we will here consider that. Huh et al. [60] divide the behavior of materials according to the extent of this amorphous zone. The films S3 and S15 are oxides, and if they are similar to tested ceramics, then the amorphous zones would be expected to be smaller than that filling up the whole specimen area of S3. It thus appears likely that the S3 ASD film can be considered amorphous and the S15 film is nanocrystalline. We also argue in the Section 3.8.6 that the electrical property observations are consistent with the S3 films being amorphous and the S5 film being polycrystalline.

We should address why the S3 ASD film is amorphous and the S15 ASD film even if we do not expect a definitive answer. From the deposition parameters of Table 1 we see that there is a large difference in the oxygen flow ratio, while as shown in Table 2 there is only a relatively small difference, if any, in the oxygen concentration in the film. That indicates close to saturation for incorporation of oxygen in the growing films. That can be compared to reports on reactive sputter deposition of NiO from a Ni target in Ar/O_2 mixtures. Hotovy et al. [61] report that their films were amorphous for a 10% mixture while crystalline for 20 and 30%, but they also pointed out that the other reports in the literature for reactive sputtering of NiO varied. Lee et al. [62] observed a similar tendency by that the crystallinity and grain size increased with increasing oxygen to argon flow ratio from 2% up to 40% and then decreased. In light of these observations the currently observed difference between the structure of S3 and S15 appears unexceptional. We also note that the voltage developed between the substrate and target was different: 198 V and 265 V respectively for S3 and S15 (see Table 1). That may be related to that it has been observed that increasing voltage have a large effect on the refinement of the columnar structure of reactively sputtering of TaN [63]. More deposition experiments covering a wider parameter space in the future are needed to understand the synthesis possibilities for the system and to find the key variable to the difference in structure between S3 and S15.

3.8.5. S3 S15 oxide discussion, $FeCoNiCuGeO_x$

The cases of reactive sputtering with oxygen containing plasma yield a nanocrystalline oxide film for S15 and an amorphous one for S3. The S3 and S15 films can both be classified as oxides by their compositions, which were relatively similar (Table 2 and Table 3). Their optical transmission had some similarities in particular their parameterized band gap. Regarding what one might expect when the elements are mixed with 50 at% or more of oxygen, we comment on the crystal structures and electronic characteristics of the different oxides found in the literature. Since J14 [15] have the elements Ni, Co and Cu in common with S3 and S15 one can expect that the elements with oxygen could exist in a NaCl structure($Fm\bar{3}m$[#225]) like NiO. The NaCl structure have remained after adding several other elements have been added to J14 including Ge, [14] i.e. $(MgCoNiCuZnGe)_1O$. We also know that $(CrFeCoNiCu)_1O$ can exist in the NaCl structure. NiO is a Mott-insulator with a wide bandgap of around 3.3–4 eV due to charge transfer from 2p of oxygen 3d state of the metal. [64, 65] FeO and CoO also exist with the same crystal structure with a bandgap of 2.4 eV. [66] and 2.2–2.8 eV [67] respectively. CuO (C2/c,#15) has a bandgap of 1.2 eV. [68] There are also reports and calculations on bandgaps of more oxygen rich oxides of the relevant metals such as Fe_2O_3 (0 eV), Ni_3O_4 (0.39 eV), Co_3O_4 (1.47 eV), CoO_2 (0.59 eV), GeO_2 (4.8 eV) [69]. In a mix of the oxides at proportions like those of S3 and S15 it is not surprising to have semiconductor or insulator behavior, even if a statistical averaging cannot be justified. One could expect to have effectively a conduction band minimum varying with position and the local mixing, and similarly for the valence band.

For S3 the structure is amorphous, so one can envision the film to have characteristics in common with amorphous semiconductors in addition to possibly local variations. A characteristic feature of an amorphous semiconductor is a tail of localized states into the band gap, and the bandgap is a mobility gap [70]. These localized tail states are involved in the carrier transport by variable range hopping and that would be in agreement with the model fit to the Efros–Shklovskii theory shown in Fig. 12(c) and presented in Section 3.6.4. That would be different for the case of the nanocrystalline S15 which showed a very high resistance. The nanocrystalline material would not have the band tails, but would likely have localized states in the band gap. These are not directly responsible for carrier transport, but can trap carriers. Any doping effect from native defects would then be compensated, and this result in no mobile charge carriers and thereby a very high resistivity.

Whether the oxides here should be classified as high entropy oxides can be debated and is a matter of definition. Whether the oxides are stabilized by entropy in an equilibrium thermodynamic sense, is an open question. Originally the concept of HEO was used for oxides which would exist in a structure/phase that was stabilized by entropy at high temperature but would decompose into other structures at lower temperatures [15, 71, 72]. Others have used the HEO term for multi-cationic equiatomic oxide systems [73, 74]. With the latter meaning of HEO sample S3 and S15 qualify as HEO, whereas for the former meaning, it is undetermined whether these oxides are stabilized by entropy in an equilibrium thermodynamic sense.

4. Conclusion

Sputter deposition from a target of FeCoNiCuGe with no intentional oxygen results in polycrystalline films with a weak 111 texture and an FCC crystal structure where the elements form a solid solution. The resistivity values of the films are higher than the Mott Regel limit and the temperature coefficient of resistivity is small (4.5 ppm/K). The sign of the Seebeck coefficient and the Hall coefficient are opposite, which is explained by both electrons and holes being at the Fermi level and contributing differently to the coefficients. The solid solution is unstable when annealing in O_2 and in forming gas above 300 °C.

Reactive sputtering with an oxygen containing plasma yields oxide films that are either nanocrystalline or amorphous dependent on the sputter conditions. These oxide films have a high transmission in the infrared and a bandgap around 1.9 eV. The amorphous film has an electrical conductance that agrees with the variable range hopping theory of Efros–Shklovskii theory

CRediT authorship contribution statement

J. Mayandi: Conceptualization, Writing – original draft, Writing – review & editing, Investigation. **T.G. Finstad:** Methodology, Writing – review & editing, Data curation. **Ø. Dahl:** Conceptualization, Writing – review & editing, Investigation. **P. Vajeeston:** Methodology, Writing – review & editing, Funding acquisition. **M. Schrade:** Writing – review & editing, Investigation. **O.M. Løvvik:** Conceptualization, Writing – review & editing. **S. Diplas:** Conceptualization, Writing – review & editing. **P.A. Carvalho:** Conceptualization, Writing – review & editing, Investigation, Project administration, Funding acquisition.

Declaration of Competing Interest

The authors declare that they have no known competing financial interests or personal relationships that could have appeared to influence the work reported in this paper."

Acknowledgments

We appreciate the help of C. Seiffert with SIMS and RBS, and G.C. Vasquez for help with SEM. This work was supported by the Research Council of Norway (Contract No. 275752 HEATER, project No.245963 Norfab, project No.197405 NORTEM, and project No. NN2875k Norwegian supercomputer).

References

[1] J.-.W. Yeh, S.-.K. Chen, S.-.J. Lin, J.-.Y. Gan, T.-.S. Chin, T.-.T. Shun, C.-.H. Tsau, S.-.Y. Chang, Nanostructured High-Entropy Alloys with Multiple Principal Elements: novel Alloy Design Concepts and Outcomes, Adv. Eng. Mater. 6 (2004) 299–303.
[2] B. Cantor, Multicomponent high-entropy Cantor alloys, Prog. Mater Sci. 120 (2021), 100754.
[3] E.J. Pickering, N.G. Jones, High-entropy alloys: a critical assessment of their founding principles and future prospects, Int. Mater. Rev. 61 (2016) 183–202.
[4] D.B. Miracle, O.N. Senkov, A critical review of high entropy alloys and related concepts, Acta Mater. 122 (2017) 448–511.
[5] E.P. George, D. Raabe, R.O. Ritchie, High-entropy alloys, Nat. Rev. Mater. 4 (2019) 515–534.
[6] S.R. Reddy, U. Sunkari, A. Lozinko, S. Guo, P.P. Bhattacharjee, Development and homogeneity of microstructure and texture in a lamellar AlCoCrFeNi2.1 eutectic high-entropy alloy severely strained in the warm-deformation regime, J. Mater. Res. 34 (2019) 687–699.
[7] S. Guo, C. Ng, J. Lu, C.T. Liu, Effect of valence electron concentration on stability of fcc or bcc phase in high entropy alloys, J. Appl. Phys. 109 (2011), 103505.
[8] D. Ma, B. Grabowski, F. Körmann, J. Neugebauer, D. Raabe, Ab initio thermodynamics of the CoCrFeMnNi high entropy alloy: importance of entropy contributions beyond the configurational one, Acta Mater. 100 (2015) 90–97.
[9] Z.G. Zhu, K.H. Ma, Q. Wang, C.H. Shek, Compositional dependence of phase formation and mechanical properties in three CoCrFeNi-(Mn/Al/Cu) high entropy alloys, Intermetallics 79 (2016) 1–11.
[10] O. Schneeweiss, M. Friák, M. Dudová, D. Holec, M. Šob, D. Kriegner, V. Holý, P. Beran, E.P. George, J. Neugebauer, A. Dlouhý, Magnetic properties of the CrMnFeCoNi high-entropy alloy, Phys. Rev. B 96 (2017), 014437.
[11] D. Bérardan, S. Franger, D. Dragoe, A.K. Meena, N. Dragoe, Colossal dielectric constant in high entropy oxides, physica status solidi (RRL), Rapid Research Letters 10 (2016) 328–333.
[12] Q. Wang, A. Sarkar, D. Wang, L. Velasco, R. Azmi, S.S. Bhattacharya, T. Bergfeldt, A. Düvel, P. Heitjans, T. Brezesinski, H. Hahn, B. Breitung, Multi-anionic and -cationic compounds: new high entropy materials for advanced Li-ion batteries, Energy Environ. Sci. 12 (2019) 2433–2442.
[13] P. Edalati, Q. Wang, H. Razavi-Khosroshahi, M. Fuji, T. Ishihara, K. Edalati, Photocatalytic hydrogen evolution on a high-entropy oxide, J. Mater. Chem. A 8 (2020) 3814–3821.
[14] H. Li, Y. Zhou, Z. Liang, H. Ning, X. Fu, Z. Xu, T. Qiu, W. Xu, R. Yao, J. Peng, High-entropy oxides: advanced research on electrical properties, Coatings 11 (2021) 628.
[15] C.M. Rost, E. Sachet, T. Borman, A. Moballegh, E.C. Dickey, D. Hou, J.L. Jones, S. Curtarolo, J.P. Maria, Entropy-stabilized oxides, Nat. Commun. 6 (2015) 8485.
[16] Y. Sharma, B.L. Musico, X. Gao, C. Hua, A.F. May, A. Herklotz, A. Rastogi, D. Mandrus, J. Yan, H.N. Lee, M.F. Chisholm, V. Keppens, T.Z. Ward, Single-crystal high entropy perovskite oxide epitaxial films, Phys. Rev. Materials 2 (2018), 060404 (R).
[17] M.R. Chellali, A. Sarkar, S.H. Nandam, S.S. Bhattacharya, B. Breitung, H. Hahn, L. Velasco, On the homogeneity of high entropy oxides: an investigation at the atomic scale, Scr. Mater. 166 (2019) 58–63.
[18] R. Djenadic, A. Sarkar, O. Clemens, C. Loho, M. Botros, V.S.K. Chakravadhanula, C. Kübel, S.S. Bhattacharya, A.S. Gandhi, H. Hahn, Multicomponent equiatomic rare earth oxides, Mater. Res. Lett. 5 (2016) 102–109.
[19] G.N. Kotsonis, C.M. Rost, D.T. Harris, J.-.P. Maria, Epitaxial entropy-stabilized oxides: growth of chemically diverse phases via kinetic bombardment, MRS Commun. 8 (2018) 1371–1377.
[20] B.R. Braeckman, F. Misják, G. Radnóczi, D. Depla, The influence of Ge and In addition on the phase formation of CoCrCuFeNi high-entropy alloy thin films, Thin. Solid. Films 616 (2016) 703–710.
[21] R. Wang, W. Chen, J. Zhong, L. Zhang, Experimental and numerical studies on the sluggish diffusion in face centered cubic Co-Cr-Cu-Fe-Ni high-entropy alloys, Journal of Materials Science & Technology 34 (2018) 1791–1798.
[22] A. Verma, P. Tarate, A.C. Abhyankar, M.R. Mohape, D.S. Gowtam, V.P. Deshmukh, T. Shanmugasundaram, High temperature wear in CoCrFeNiCux high entropy alloys: the role of Cu, Scr. Mater. 161 (2019) 28–31.
[23] M. Arfaoui, G. Radnóczi, V.Kovács Kis, Transformations in CrFeCoNiCu High Entropy Alloy Thin Films during In-Situ Annealing in TEM, Coatings 10 (2020) 60.
[24] M. Schrade, H. Fjeld, T. Norby, T.G. Finstad, Versatile apparatus for thermoelectric characterization of oxides at high temperatures, Rev. Sci. Instrum. 85 (2014), 103906.
[25] D.C. Bufford, Y.M. Wang, Y. Liu, L. Lu, Synthesis and microstructure of electrodeposited and sputtered nanotwinned face-centered-cubic metals, MRS Bull. 41 (2016) 286–291.
[26] L.R. Owen, H.J. Stone, H.Y. Playford, The assessment of local lattice strains in alloys using total scattering, Acta Mater. 170 (2019) 38–49.
[27] C.V. Thompson, Grain growth in thin films, Annu. Rev. Mater. Sci. 20 (1990) 245–268.
[28] C.V. Thompson, Structure evolution during processing of polycrystalline films, Annu. Rev. Mater. Sci. 30 (2000) 159–190.
[29] T.F. Yi, T.T. Wei, J. Mei, W. Zhang, Y. Zhu, Y.G. Liu, S. Luo, H. Liu, Y. Lu, Z. Guo, Approaching high-performance supercapacitors via enhancing pseudocapacitive nickel oxide-based materials, Adv. Sustain. Syst. 4 (2020), 1900137, https://doi.org/10.1002/adsu.201900137.
[30] Z. Kozakova, I. Kuritka, P. Bazant, M. Pastorek, V. Babayan, Magnetic needle-like iron oxide particles prepared by microwave-assisted thermal decomposition technique, Mater. Lett. 138 (2015) 116–119.
[31] Q. Guan, J. Cheng, B. Wang, W. Ni, G. Gu, X. Li, L. Huang, G. Yang, F. Nie, Needle-like Co3O4 anchored on the graphene with enhanced electrochemical performance for aqueous supercapacitors, ACS Appl. Mater. Interfaces 6 (2014) 7626–7632.
[32] J. Mayandi, T.G. Finstad, M. Stange, M. F.Sunding, O.M. Løvvik, S. Diplas, P. A. Carvalho, Controlling the electrical properties of reactively sputtered high entropy alloy CrFeNiCoCu films, J. Electron. Mater. (2021), https://doi.org/10.1007/s11664-021-09343-3.
[33] N.E. Hussey, K. Takenaka, H. Takagi, Universality of the Mott-Ioffe-Regel limit in metals, Philos. Mag. 84 (2004) 2847.
[34] H. Song, F. Tian, Q.-.M. Hu, L. Vitos, Y. Wang, J. Shen, N. Chen, Local lattice distortion in high-entropy alloys, Phys. Rev. Mater. 1 (2017), 023404.
[35] R.J. Goetsch, V.K. Anand, A. Pandey, D.C. Johnston, Structural, thermal, magnetic, and electronic transport properties of the $LaNi_2(Ge_{1-x}P_x)_2$ system, Phys. Rev. B. 85 (2012), 054517, https://doi.org/10.1103/PhysRevB.85.054517.
[36] N.F. Mott, M. Kaveh, Metal-insulator transitions in non- crystalline systems, Adv. Phys. 34 (1985) 329–401.
[37] S.A. Hartnoll, Theory of universal incoherent metallic transport, Nat. Phys. 11 (2014) 54–61.
[38] S. Shafeie, S. Guo, P. Erhart, Q. Hu, A. Palmqvist, Balancing scattering channels: a panoscopic approach toward zero temperature coefficient of resistance using high-entropy alloys, Adv. Mater. 31 (2019), e1805392.
[39] M.A. Park, Y.J. Kim, Weak-localization effect in superconductors from radiation damage, Phys.Rev.B 61 (2000) 14733.
[40] J. Kondo, Resistance minimum in dilute magnetic alloys, Prog. Theor. Phys. 32 (1964) 37.
[41] S. Baranovskii, O. Rubel, Charge transport in disordered materials, in: S. Kasap, P. Capper (Eds.), Springer Handbook of Electronic and Photonic Materials, Springer Handbooks. Springer, Cham, 2017, https://doi.org/10.1007/978-3-319-48933-9_9.
[42] N.F. Mott, Conduction in non-crystalline materials, Philos. Mag. 19 (1969) 835–852.
[43] A.L. Efros, B.I. Shklovskii, Coulomb gap and low temperature conductivity of disordered systems, J. Phys. C Solid State Phys. 8 (4) (1975) L49.
[44] T.C. Chasapis, D. Koumoulis, B. Leung, N.P. Calta, S.H. Lo, V.P. Dravid, L. S. Bouchard, M.G. Kanatzidis, Two-band model interpretation of the p- to n-transition in ternary tetradymite topological insulators, APL Mater 3 (2015), 083601.
[45] G. Kresse, J. Furthmüller, Efficient iterative schemes for ab initio total-energy calculations using a plane-wave basis set, Phys. Rev. B 54 (1996) 11169–11186.
[46] G. Kresse, D. Joubert, From ultrasoft pseudopotentials to the projector augmented-wave method, Phys. Rev. B 59 (1999) 1758–1775.
[47] J.P. Perdew, K. Burke, M. Ernzerhof, Generalised gradient approximation made simple, Phys. Rev. Lett. 77 (1996) 3865–3868.
[48] A. Zunger, S.H. Wei, L.G. Ferreira, J.E. Bernard, Special quasirandom structures, Phys. Rev. Lett. 65 (1990) 353–356.
[49] A. van de Walle, P. Tiwary, M. de Jong, D.L. Olmsted, M. Asta, A. Dick, D. Shin, Y. Wang, L.-.Q. Chen, Z.-.K. Liu, Efficient stochastic generation of special quasirandom structures, Calphad 42 (2013) 13–18, https://doi.org/10.1016/j.calphad.2013.06.006.

[50] T.S. Reddy, M.C.S. Kumar, Co3-evaporated SnS thin films for visible light photodetector applications, RSC Adv. 6 (2016) 95680–95692.
[51] I. Chambouleyron, J.M. Martínez, Handbook of Thin Film Materials, 2001, pp. 593–622. H.S. Nalwa Ed. (Academic, San DiegoVol. 3, pp.
[52] P.M. Agrawal, B.M. Rice, D.L. Thompson, Predicting trends in rate parameters for self-diffusion on FCC metal surfaces, Surf. Sci. 515 (2002) 21–35.
[53] O. Anderoglu, A. Misra, H. Wang, X. Zhang, Thermal stability of sputtered Cu films with nanoscale growth twins, J. Appl. Phys. 103 (2008), 094322.
[54] G. Vetterick, J.K. Baldwin, A. Misra, M.L. Taheri, Texture evolution in nanocrystalline iron films deposited using biased magnetron sputtering, J. Appl. Phys. 116 (2014), 233503.
[55] D.G. Neerinck, A.E.M. De Veirman, M.H.J. Slangen, T.G.S.M. Rijks, J.C.S. Kools, Grain size and strain in thin sputter-deposited N0.8Fe0.2 and Cu films, Thin. Solid. Films 280 (1996) 136–141.
[56] A. Dulmaa, F.G. Cougnon, R. Dedoncker, D. Depla, On the grain size-thickness correlation for thin films, Acta Mater. 212 (2021).
[57] J. Dąbrowa, M. Zajusz, W. Kucza, G. Cieślak, K. Berent, T. Czeppe, T. Kulik, M. Danielewski, Demystifying the sluggish diffusion effect in high entropy alloys, J. Alloys Compd. 783 (2019) 193–207.
[58] A. Vida, L.K. Varga, N.Q. Chinh, D. Molnar, S. Huang, L. Vitos, Effects of the sp element additions on the microstructure and mechanical properties of NiCoFeCr based high entropy alloys, Mater. Sci. Eng. 669 (2016) 14–19.
[59] X. Ou, Molecular dynamics simulations of fcc-to-bcc transformation in pure iron: a review, Mater. Sci. Technol. 33 (2016) 822–835.
[60] Y. Huh, K.J. Hong, K.S. Shin, Amorphization induced by focused ion beam milling in metallic and electronic materials, Microsc. Microanal. 19 (Suppl 5) (2013) 33–37.
[61] I. Hotovy, D. Buc, S. Hascik, O. Nennewitz, Characterization of NiO thin films deposited by reactive sputtering, Vacuum 50 (1998) 41–44.
[62] J.W. Lee, I.H. Park, C.W. Chung, Electrical characterization of nickel oxide thin films deposited by reactive sputtering for memory applications, Integr. Ferroelectr. 74 (2006) 71–77.
[63] W. Dai, Y. Shi, Effect of bias voltage on microstructure and properties of tantalum nitride coatings deposited by RF magnetron sputtering, Coatings 11 (2021) 911.
[64] M.D. Irwin, D.B. Buchholz, A.W. Hains, R.P.H. Chang, T.J. Marks, p-Type semiconducting nickel oxide as an efficiency-enhancing anode interfacial layer in polymer bulk-heterojunction solar cells, Proc. Natl. Acad. Sci. 105 (2008) 2783–2787.
[65] A.C. Gandhi, S.Y. Wu, Strong deep-level-emission photoluminescence in NiO Nanoparticles, Nanomaterials (Basel) 7 (2017) 231.
[66] R. Ashraf, T. Mahmood, S. Riaz, S. Naseem, Study of the structural and electronic properties of FeO at the LDA and GGA level, Chin. J. Phys. 55 (2017) 1135–1141.
[67] A. Matsuda, R. Yamauchi, D. Shiojiri, G. Tan, S. Kaneko, M. Yoshimoto, Room-temperature selective epitaxial growth of CoO (1 1 1) and Co3O4 (1 1 1) thin films with atomic steps by pulsed laser deposition, Appl. Surf. Sci. 349 (2015) 78–82.
[68] N.R. Dhineshbabu, V. Rajendran, N. Nithyavathy, R. Vetumperumal, Study of structural and optical properties of cupric oxide nanoparticles, Appl. Nanosci. 6 (2015) 933–939.
[69] A. Jain, S.P. Ong, G. Hautier, W. Chen, W.D. Richards, S. Dacek, S. Cholia, D. Skinner D.Gunter, G. Ceder, K.A. Persson, The Materials Project: a materials genome approach to accelerating materials innovation, APL Mater. 1 (2013), 011002, https://doi.org/10.1063/1.4812323.
[70] K. Morigaki, C. Ogihara, Amorphous semiconductors: structure, optical, and electrical properties, in: S. Kasap, P. Capper (Eds.), Springer Handbook of Electronic and Photonic Materials, Springer Handbooks. Springer, Cham, 2017, https://doi.org/10.1007/978-3-319-48933-9_24.
[71] G. Anand, A.P. Wynn, C.M. Handley, C.L. Freeman, Phase stability and distortion in high-entropy oxides, Acta Mater. 146 (2018) 119–125.
[72] A. Sarkar, Q. Wang, A. Schiele, M.R. Chellali, S.S. Bhattacharya, D. Wang, T. Brezesinski, H. Hahn, L. Velasco, B. Breitung, High-entropy oxides: fundamental aspects and electrochemical properties, Adv. Mater. 31 (2019), e1806236.
[73] D. Bérardan, S. Franger, A.K. Meena, N. Dragoe, Room temperature lithium superionic conductivity in high entropy oxides, J. Mater. Chem. A 4 (2016) 9536–9541.
[74] D. Berardan, A.K. Meena, S. Franger, C. Herrero, N. Dragoe, Controlled Jahn-Teller distortion in (MgCoNiCuZn)O-based high entropy oxides, J. Alloys Compd. 704 (2017) 693–700.